ABSTRACT

Title of dissertation: EXPERIMENTS IN
TWO-MODE CAVITY QED

David Glenn Norris, Doctor of Philosophy, 2011

Dissertation directed by: Professor Luis Orozco
Department of Physics

Cavity quantum electrodynamics (QED) allows the study of light-matter interactions at the most basic level, through precise identification of the coherent and incoherent (dissipative) parts of the system evolution. We present measurements of light from a cavity QED system consisting of a high-finesse optical resonator coupled to a beam of cold Rb atoms. The novelty of the design lies in the interplay of two degenerate and orthogonal polarization modes. One mode (driven) behaves as the canonical cavity mode of the Jaynes-Cummings Hamiltonian, coherently exciting the atoms with a modest coupling strength; the other mode (undriven) collects a small fraction of spontaneously emitted light and provides a probe of the dissipative processes.

We first demonstrate the ability to detect individual atoms passing through the cavity modes in real time by coincidence detection of photons from the undriven mode. Calculation of statistics and correlation functions from the complete photon detection record allows the determination of detection probabilities and the reconstruction of atomic trajectories. We next present evidence of quantum coher-

ence that is created, modified, and measured in the excitation-spontaneous emission cycle. The coherence appears as a long-lived quantum beat at the ground-state Larmor frequency, visible in the intensity autocorrelation function of the undriven mode. Quantum jumps of the atomic state, occurring in between the detections of photons from the cavity, result in substantial changes in the frequency and spectral width of the beats. We present the results of a full quantum Monte Carlo calculation in order to quantitatively explain the measurements.

EXPERIMENTS IN TWO-MODE CAVITY QED

by

David Glenn Norris

Dissertation submitted to the Faculty of the Graduate School of the
University of Maryland, College Park in partial fulfillment
of the requirements for the degree of
Doctor of Philosophy
2011

Advisory Committee:
Professor Luis A. Orozco, Chair/Advisor
Professor Howard J. Carmichael
Professor Mario Dagenais
Professor William D. Phillips
Professor Steven L. Rolston

Acknowledgments

The work presented in this thesis is the product of six years of collaborative effort. The largest debt of gratitude is owed to my advisor and mentor, Professor Luis Orozco, who has most greatly shaped my development as a physicist. I know of no one more committed to science and to inculcating a respect for science in his students. Another great deal is owed to Professor Howard Carmichael, whose year with us proved crucial to understanding the physics involved in this work. The instruction happened chiefly over coffee, and I am privileged to count such a brilliant person as teacher and friend.

Many others have contributed to this project over the years, including current and former members of the UMD cavity QED group (Michael Scholten, Basudev Roy, Rebecca Olson Knell, Matt Terraciano, and Andres Cimmarusti, in whose capable hands I leave the apparatus); our former postdoctoral researcher, Jietai Jing; our undergraduate researchers, Josh Crawford and Eric Cahoon; and a host of visiting student researchers. In addition, we have benefited from theory collaboration with Pablo Barberis in Mexico, and Perry Rice and James Clemens in Ohio.

Finally, I expressly acknowledge the contributions of the National Science Foundation, which has supported me monetarily for the past six years through a Graduate Research Fellowship, grants to the cavity QED program, and establishment of the Physics Frontier Center at the Joint Quantum Institute. Their generous funding made this research possible.

Table of Contents

List of Figures

List of Abbreviations

AM	amplitude modulation
AOM	acousto-optic modulator
APD	avalanche photodiode
DAVLL	dichroic absorption vapor laser lock
DC	direct current
EOM	electro-optic modulator
FM	frequency modulation
FSR	free spectral range
FWHM	full width at half maximum
HWP	half-wave plate
JC	Jaynes-Cummings
LVIS	low-velocity intense source
MOT	magneto-optical trap
NIM	nuclear instrumentation module
PBS	polarizing beam splitter
PDH	Pound-Drever-Hall
PID	proportional-integral-differential
PMT	photomultiplier tube
PZT	piezo-electric transducer
QED	quantum electrodynamics
RF	radio frequency
TEM	transverse electromagnetic
TTL	transistor-transistor logic

Chapter 1

Two-Mode Cavity Quantum Electrodynamics

1.1 Introduction

A cavity quantum electrodynamic (QED) system consists of an atom or other quantum object coupled to a small number of modes of a cavity [1]. Such a system provides a simple structure in which to investigate fundamental aspects of matter-light interactions, and may also be used for applications in quantum information science [2, 3, 4, 5]. Several cavity QED geometries operating over a wide range of the electromagnetic spectrum have now been demonstrated experimentally (see for example [1, 6, 7, 8].)

This thesis presents a collection of experiments performed on a particular cavity QED system, a two-mode optical cavity and cold atomic source first described in [9] and [10]. We begin with a theoretical overview of the system and the measurement goals. As the basic setup is common to all of the experiments discussed in this thesis, we give a thorough account of the technical details in this chapter, with additional details for each specific measurement in the subsequent chapters.

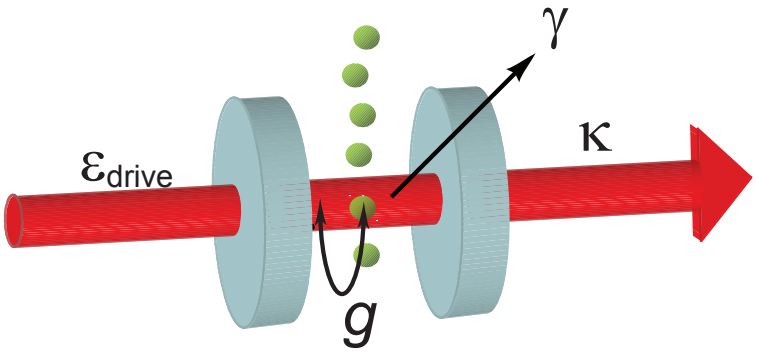

Figure 1.1: The optical cavity QED system. g: atom-photon dipole coupling frequency; γ: free-space atomic decay rate; κ: cavity field mode decay rate; $\mathcal{E}_{\text{drive}}$: coherent driving field amplitude.

1.2 Theoretical models

1.2.1 The Jaynes-Cummings model

The Jaynes-Cummings (JC) model provides the simplest realization of quantized light-atom interactions [11]. The model considers a single two-level atom, a saturable absorber, coupled to a mode of the electromagnetic field, a harmonic oscillator of equally-spaced energy levels; the mode is typically defined by the mirror boundaries in an optical cavity (see Fig. 1.1.) Coherent electric-dipole coupling between the atom and a single photon (an excitation quantum of the mode) takes place at the Rabi frequency

$$g = \mu E/\hbar = \frac{\mu}{\hbar}\sqrt{\frac{\hbar\omega_c}{2\epsilon_0 V}}, \tag{1.1}$$

where μ is the atomic transition dipole moment and E is the amplitude of the electric field of a single photon, with mode volume V and frequency ω_c. The system

Hamiltonian without dissipation is

$$H_{JC} = \hbar\omega_a\sigma_z + \hbar\omega_c a^\dagger a - i\hbar g(\sigma_+ a - a^\dagger\sigma_-). \tag{1.2}$$

Here ω_a is the natural atomic transition frequency, a is the annihilation operator for the cavity field, and $\sigma_{\pm,z}$ are the Pauli spin operators for a two-level atom. The evolution in this case is simply a continuous, reversible exchange of energy between the atom and the cavity mode.

Dissipation may be added by considering separate reservoirs coupled to the cavity mode and atomic radiation pattern. Once traced over, non-reversible decay into these reservoirs brings lifetimes $1/\kappa$ and $1/\gamma$ for the cavity field and atomic excited state population, respectively [12]. The effect of a single photon on the atomic state is characterized by the saturation photon number, $n_{\rm sat} \equiv \gamma^2/(8g^2)$, which may reach values much less than one for sufficiently strong coupling. The effect of an atom on the cavity field is similarly characterized by the single-atom cooperativity parameter, $C_1 \equiv g^2/(\kappa\gamma)$, which expresses the ratio of coherent coupling to dissipation rates. For the case of N atoms coupled identically to the mode, constructive interference enhances the emissions into the cavity mode, and the cooperativity parameter increases to $C = NC_1$ [13].

Driving the cavity on resonance with a laser field of amplitude $\mathcal{E}_{\rm drive}$ (outside the cavity) causes the build-up of a coherent field inside the cavity, the amplitude of which depends on C. The steady-state behavior of the system is given by the state equation, first introduced in the context of optical bistability [13]:

$$Y = X(1 + 2C/(1 + X))^2, \tag{1.3}$$

where Y is the intracavity photon number without atoms, and X is the number with atoms (both are normalized to n_{sat}.) This form is exact for a plane-wave mode in a traveling-wave (ring) cavity, and it exhibits bistable behavior for large values of C and X. In the limit of weak driving ($X \ll 1$), the equation takes on the simpler form:

$$Y = X(1 + 2C)^2. \tag{1.4}$$

This equation shows that X is smaller than Y by the factor $1/(1 + 2C)^2$, primarily due to the drive light radiated into free space by the atoms.

1.2.2 JC model versus reality

Experimental realization of the JC Hamiltonian entails a number of approximations. True two-level atomic systems are rare. Even the alkalis, a staple of atomic physics experiments because of their relatively simple spectra, exhibit complicated magnetic hyperfine structure and are susceptible to optical pumping. An example is the ^{85}Rb D_2-line $F = 3 \rightarrow F' = 4$ manifold shown in figure Fig. 1.2a. An effective two-level atom in such a level structure can be realized experimentally by optically pumping to the $F = 3, m = +3(-3)$ ground state and using a σ^+ (σ^-) circularly polarized cavity mode to drive the $F = 3, m = +3(-3) \rightarrow F' = 4, m' = +4(-4)$ cycling transition, provided that light polarization and magnetic fields are carefully controlled.

Real cavity mode structure is likewise complicated. In a standing-wave cavity of length l and in the transverse electromagnetic (TEM) basis, longitudinal modes

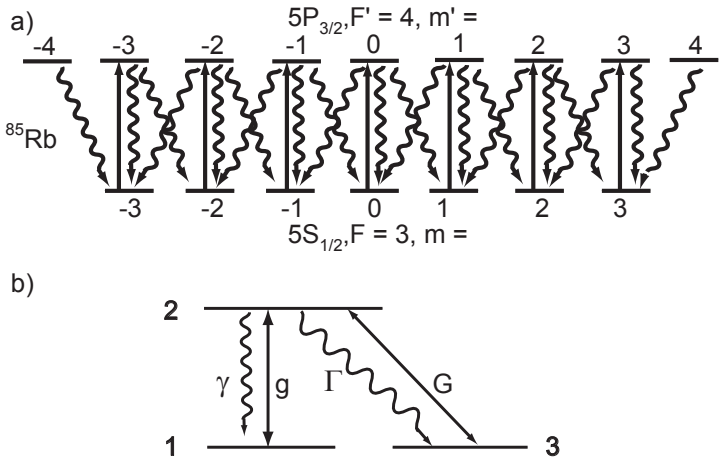

Figure 1.2: a) Diagram of ^{85}Rb levels used in the experiments. b) Simplified three-level atomic model with coupling constants for the two cavity modes.

are separated by a free spectral range, FSR $= c/2l$, with each of these split into multiple transverse modes. The requirement of a single spatial mode in the JC model means that all other modes must be separated from the mode of interest by several cavity linewidths. In addition, each transverse mode supports two orthogonal polarizations. The frequency splitting between the modes is determined by the rate of cross-coupling between polarizations due to cavity mirror birefringence. True single-mode excitation is accomplished by driving one of the polarization eigenmodes (generally elliptically polarized), but for sufficiently small birefringence an arbitrary polarization may be used.

A greater and still outstanding problem experimentally is keeping a single atom localized in the cavity mode within a region of much less than one half-wavelength, such that the value of g, which varies spatially with the mode structure of E, is

constant and known. Early cavity QED experiments operated with a thermal beam of atoms, giving a random and changing distribution of coupling strengths and atom number, and non-adiabatic interaction dynamics due to the high speeds [14]. Individual neutral atoms trapped inside a cavity mode have been demonstrated, but still with time-varying values of g and a substantial warping of the level structure due to light shifts [15, 16]. Single ions trapped in a cavity hold more promise, but face their own technical challenge owing to the close presence of dielectric mirrors [17].

Our goal in this work is to explore the dynamics of a real cavity QED system in full quantitative detail beyond the limits of the single-mode JC Hamiltonian. The atoms are multitudinous and freely moving, but can be reduced in number to allow detection and manipulation of individual atoms. The magnetic structure entails all sixteen levels shown in Fig. 1.2a, and supports the creation of ground-state coherence that does not exist for two-level atoms. The cavity birefringence is small enough to permit two degenerate polarization modes, but large enough to give substantial contributions to the measured signals.

We first consider a simple extension to the JC model in order to motivate the measurements that follow. In the subsequent chapters we will introduce greater complexity into the model, requiring a quantum Monte Carlo simulation for the full calculations.

1.2.3 Two modes and three levels

As a first complication, we consider a three-level Λ-type atom (Fig. 1.2b) inside a cavity with two orthogonal and degenerate polarization eigenmodes, with annihilation operators a and b ([10]). The $|1\rangle$-to-$|2\rangle$ transition dipole couples to a photon in mode a with Rabi frequency g, and the $|2\rangle$-to-$|3\rangle$ transition dipole couples to a photon in mode b with Rabi frequency G. The total spontaneous emission rate is the sum of the emission in the two channels, $\gamma_{\rm tot} = \gamma + \Gamma$. The atom starts in state $|1\rangle$ and the excitation is sufficiently weak such that the probability of being transferred to state $|3\rangle$ and subsequently re-excited by the driving light is negligibly small. This avoids the problem that the atom in Fig. 1.2b gets pumped to a dark state of the driving laser (π polarization), while the real level structure in Fig. 1.2a has no dark states.

The cavity is driven with a coherent field (inside the cavity) of amplitude ε in mode a. The effective Hamiltonian in between quantum jumps and in the rotating-wave approximation is [12, 10]:

$$\begin{aligned} H_{mode} &= \frac{\varepsilon}{\kappa}\left(a - a^\dagger\right) + i\hbar g\left(a\sum_{i=1}^{N}|2\rangle_i\langle 1| - a^\dagger\sum_{i=1}^{N}|1\rangle_i\langle 2|\right) \\ &\quad + i\hbar G\left(b\sum_{i=1}^{N}|2\rangle_i\langle 3| - b^\dagger\sum_{i=1}^{N}|3\rangle_i\langle 2|\right) \\ &\quad - i\hbar\kappa\left(a^\dagger a + b^\dagger b\right) - i\hbar\frac{\gamma+\Gamma}{2}\sum_{i=1}^{N}|2\rangle_i\langle 2|, \end{aligned} \tag{1.5}$$

where the sums are over the N atoms, each considered to be identically coupled to the mode.

We now have two single-atom cooperativity parameters, $C_1 = g^2/(\kappa\gamma_{\rm tot})$ for

the driven mode and $\widetilde{C}_1 = G^2/(\kappa\gamma_{\rm tot})$ for the orthogonal mode. The effect of $\widetilde{C}_1$ on the driven mode is to reduce the cooperativity by an amount commensurate with emission into the orthogonal mode; instead of $C = NC_1$, we define a new driven mode cooperativity,

$$C' = \frac{C_1 N}{1 + 2\widetilde{C}_1}. \tag{1.6}$$

Defining separate values of the intracavity photon number X for the driven ($X_\parallel$) and orthogonal ($X_\perp$) modes, the state equations become [10]:

$$X_\parallel = Y\frac{1}{(1+2C')^2} \approx Y\left(1 - 4C'\right), \tag{1.7}$$

$$X_\perp = Y\left[\frac{2\widetilde{C}_1}{1+2\widetilde{C}_1}\right]\left[\frac{C'}{(1+2C')^2}\right] \approx Y 2\widetilde{C}_1 C', \tag{1.8}$$

where the lowest-order approximations are valid for $2C \ll 1$ and $2\widetilde{C}_1 \ll 1$, and we assume weak drive ($X \ll 1$). The population of the driven mode decreases with C' as before, while the population of the orthogonal mode increases with C'; in other words, $X_\perp$ contains a fraction of the light $Y - X_\parallel$ that would otherwise have been radiated into free space.

This thesis studies light emission from the two modes for a variety of experimental parameters. In particular, we study time-resolved photon correlation measurements of light from $X_\perp$, which reveal information on atomic dynamics and coherences that are invisible in the steady-state average.

1.3 Apparatus

1.3.1 Physics cavity

We perform measurements on light escaping from a high-finesse Fabry-Perot interferometer (referred to below as the "physics cavity".) The mirrors that form the cavity have reflective coatings from Research Electro-Optics of Boulder, CO, with transmissions $T_1 = 15$ ppm and $T_2 = 270$ ppm at a wavelength of $\lambda = 780$ nm, where the larger transmission T_2 corresponds to the mirror on the output side [9]. The spacing between the reflective surfaces is $l = 2.2$ mm, and the mirrors have radii of curvature 25 cm and 10 cm, respectively. The cavity supports a TEM_{00} mode with $1/e$ field waist $w_0 = 56$ μm and Rayleigh range $\pi w_0^2/\lambda = 1.2$ cm, i.e. the mode diameter changes little over the distance between the mirrors. The cavity free spectral range is $\mathrm{FSR} = c/(2l) = 68$ GHz.

Barring additional losses, we expect cavity finesse $\mathcal{F} = 2\pi/(T_1 + T_2) = 22\,000$ and resonance full width at half maximum (FWHM) $2\kappa/(2\pi) = \mathrm{FSR}/\mathcal{F} = 3.1$ MHz. We measure instead a FWHM of 5.8 MHz and a finesse of $\mathcal{F} = 12\,000$. We infer from this an additional loss channel approximately equal in magnitude to the larger mirror transmission. This loss is most likely due to residual glue deposited on the mirror surface during construction. When inferring the photon number inside the cavity, we increase our estimate by a factor of two due to this loss. This agrees with the results of full Quantum Monte Carlo simulations of the system discussed in Chapter 3. The cavity also has a small intrinsic birefringence, which results in a slight (less than 200 kHz) splitting between the two (elliptical) polarization

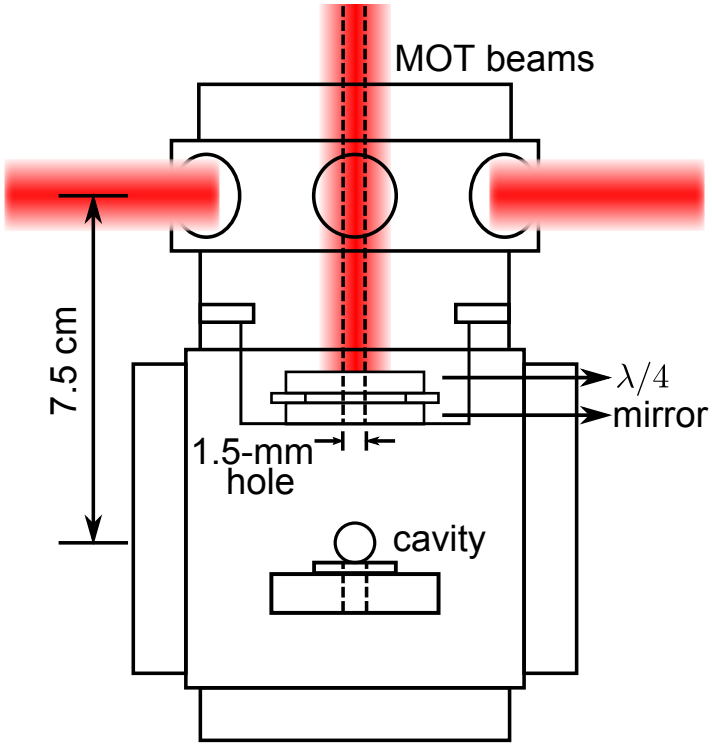

Figure 1.3: Schematic (not to scale) of vacuum chamber containing optical cavity and LVIS apparatus.

eigenmodes. Because this splitting is much less than $\kappa/(2\pi)$, we can effectively choose an arbitrary polarization basis for driving the cavity (typically vertical and horizontal) and suffer only a small background of coherent light in the undriven mode due to birefringence coupling.

The cavity length is controlled by two shear piezo-electric transducers (PZT) to which the mirrors are glued. The PZT's are glued to a stainless steel base, which rests on a stack of alternating layers of Sorbothane (a synthetic polymer from Sorbothane, Inc.) and lead for acoustic isolation [18]. The unit resides in a small stainless steel vacuum chamber at 10^{-8} Torr (Fig. 1.3), with electrical feedthroughs

for the PZT's. One PZT is driven by the amplified output of a Stanford Research Systems SIM960 Proportional-Integral-Differential (PID) controller, with a feedback bandwidth of about 1 kHz. The other PZT is connected to a high-voltage direct current (DC) power supply to correct for slow thermal drift. A LabVIEW program monitors the output of the PID controller and adjusts the DC voltage to keep the error signal output near zero. The power supply voltage spans about three cavity FSR's.

1.3.2 Atomic source

We extract a continuous cold beam of ^{85}Rb atoms from a modified magneto-optical trap (MOT). The atoms are supplied by a Rb dispenser from SAES Getters, Inc., operated at a current of 3.4 A. The trap uses a pair of coils in near "anti-Helmholtz" configuration (8 cm diameter and 5 cm separation) to produce a magnetic field gradient of 10 G/cm. We cool the atoms with three orthogonal retro-reflected beams at 780 nm tuned below the $F = 3 \rightarrow F' = 4$ cycling transition. Each beam has a power of approximately 15 mW and a diameter of 2 cm. The detuning from resonance is approximately -20 MHz, which we vary by changing the frequency of a double-passed acousto-optic modulator (AOM). The exact parameters are optimized to give the greatest flux of atoms. A repumping beam resonant with transitions from the F =2 ground state to the $F' = 3$ or 4 excited states is mixed with the MOT beams on a polarizing beam splitter (PBS).

The atoms exit via a 1.5 mm-diameter hole in the vertical beam retro-reflecting

optic, which consists of a quarter-wave plate ($\lambda/4$) atop a gold mirror, placed at the bottom of the MOT chamber. The radiation imbalance above the hole pushes out a continuous beam of atoms in a Low-Velocity Intense Source (LVIS) configuration [19]. The atoms have a mean longitudinal velocity of about 20 m/s, determined from comparison of measured data with Monte Carlo simulation (see Chapter 3.) The beam intersects the cavity mode at near normal incidence, 3-4 cm below the hole in the mirror. We estimate a maximum flux of about 1×10^7 atoms s^{-1} that pass through the cavity mode, corresponding to a mean mode occupation of 50 atoms with an average transit time of 5 μs. For some measurements, we reduce the flux of atoms in order to have a mean mode occupation of less than one atom. This is accomplished by changing the detuning or power of the MOT beams.

As part of the measurements, we require control of the magnetic field inside the cavity, in particular the components parallel to the input laser polarization (vertical) and parallel to the cavity axis (horizontal). To adjust the field in the vertical direction, we implement a third coil below the "anti-Helmholtz" coil pair. This allows us to vary the field in the cavity between $\pm$ 12 G (corresponding to a splitting between ground-state Zeeman levels of approximately $\gamma/2$) while affecting the field in the MOT region only slightly. We use an additional pair of coils oriented with axis parallel to the cavity axis to control the magnetic field in that direction as well.

Coming out of the MOT in LVIS configuration with a vertical magnetic field applied, the atoms are left primarily in the $m = 3$ ground state, with the exact distribution sensitive to laser alignment and detuning. Before they enter the cavity

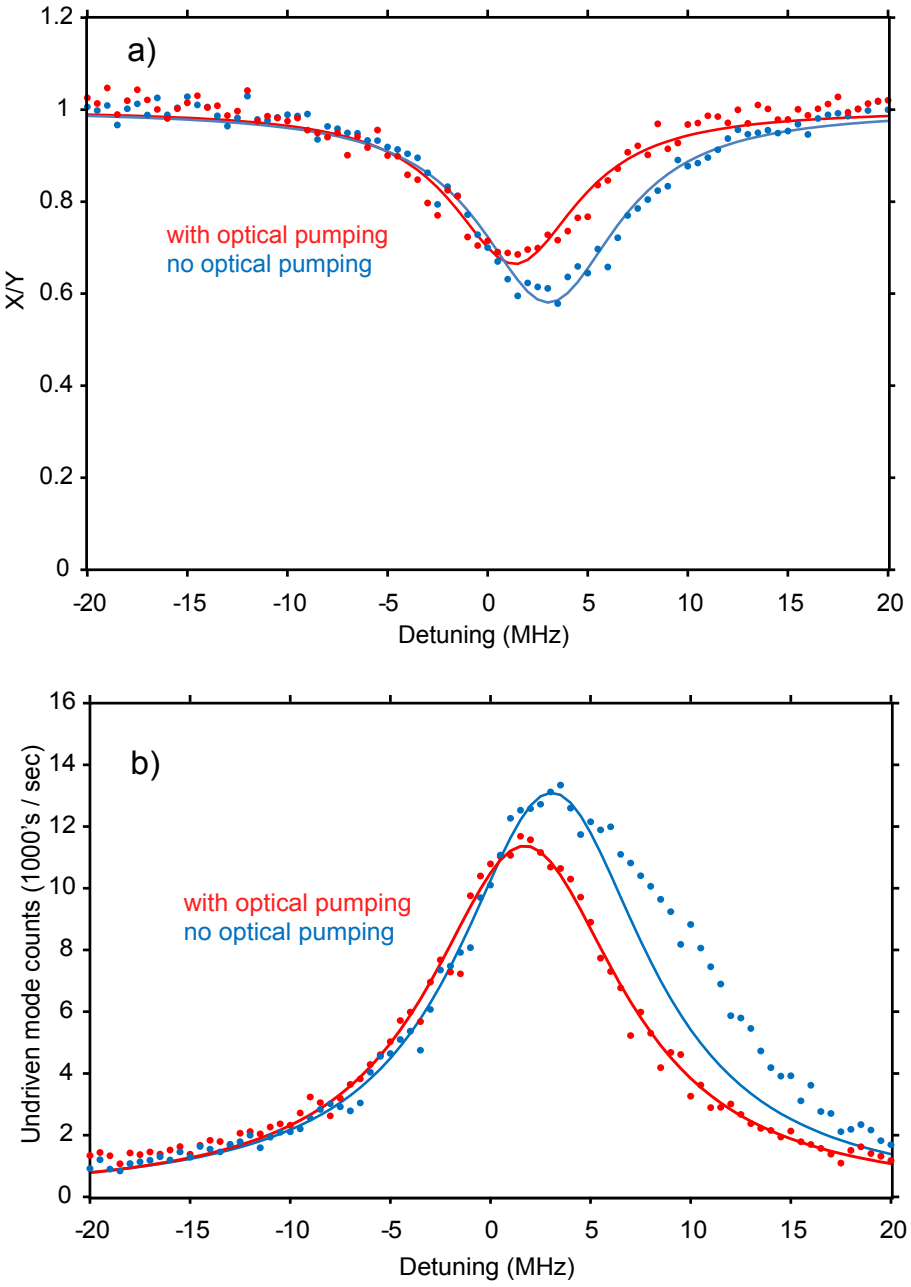

Figure 1.4: a.) Example of absorption fraction X/Y in driven mode as a function of common detuning of laser and cavity frequency from central m =0 to m' =0 transition. The optical pumping beam shifts the population toward the center. The magnetic field value is approximately 5 G and drive strength is approximately one photon in the cavity, with drive polarization parallel to the magnetic field. Solid lines are least-square fits of the data points to a Lorentzian line shape. b.) Count rates from the undriven mode measured concurrently with data in (a), with Lorentzian fits.

mode, we optically pump the atoms to the $m = 0$ state using a beam resonant with the $F = 3 \rightarrow F' = 3$ transition and with polarization vector parallel to the vertical magnetic field. The beam is combined with light from the repumper laser in a 50/50 polarization-maintaining single-mode fiber splitter, and collimated to a waist diameter of 0.5 mm in order to pass between the top of the cavity mirrors and the upper edge of the viewport. Due to strong scattering into the photon detectors from multiple reflections, we are unable to use the beam in a retro-reflected configuration. Therefore, the beam imparts a net momentum kick to the atoms, which must be compensated for with atomic beam alignment. Alternatively, a configuration of MOT beams may be found which leaves a broader distribution of population over the ground states. In this case the optical pumping beam acts as a filter, ejecting those atoms which are not already in $m = 0$. The intensity of the optical pumping beam and repumper are optimized as a compromise between moving most of the atoms to $m = 0$ while not ejecting too many from the beam.

Figure 1.4 shows a typical measurement sequence used for optimization of the optical pumping beam. The effect of the beam is to shift and narrow the line shapes for both absorption and emission, with the goal of having narrow Lorentzian peaks centered around 0 MHz (the resonance frequency of the $F = 3, m = 0 \rightarrow F' = 4, m' = 0$ transition.) The distributions do not always shift completely to the center (an effect evident in Fig. 1.4); this is likely due to some combination of incomplete optical pumping and a small ($\sim$ 1 MHz) drift in the frequency setpoint of the saturated absorption spectroscopy reference, arising from temperature-dependent amplitude modulation (AM) in the electro-optic modulator (EOM) that generates

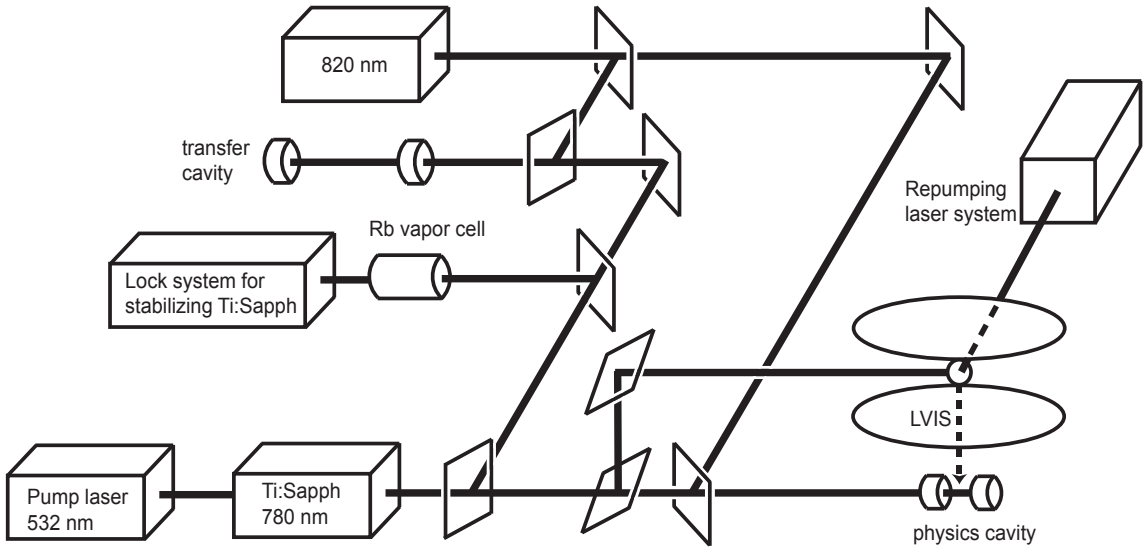

Figure 1.5: Schematic of the laser system used for stabilizing and probing the optical cavity, and for cooling and trapping the atoms.

frequency modulation (FM) sidebands for the error signal (see below).

1.3.3 Laser system

Figure 1.5 shows a schematic of the apparatus, focusing on the laser system. The primary source of light at 780 nm is a Titanium:Sapphire MBR-110 laser (Ti:Sapph), driven by a 10 W pump laser at 532 nm (Verdi V-10), both from Coherent, Inc. A reference cavity-based lock internal to the MBR housing narrows the Ti:Sapph linewidth to less than 100 kHz. Long-term frequency stability and absolute frequency referencing are accomplished by saturated-absorption spectroscopy in a magnetically-shielded Rb vapor cell. The error signal is derived from the ^{85}Rb $F = 3 \rightarrow (F' = 3, F' = 4)$ hyperfine crossover transition. We generate the signal by imprinting FM sidebands at 12 MHz with an EOM, detecting the saturated ab-

sorption with a fast photodiode, and mixing the amplified photodiode output with the radio frequency (RF) local oscillator. Locking is accomplished with a SIM960 PID controller, the output of which is fed to the external scan input on the MBR control box. The light output of the MBR at this frequency is approximately 1 W.

We stabilize the length of the physics cavity with a Toptica DL-100 diode laser at 820 nm, which interacts negligibly with the atomic beam but still reflects strongly from the cavity mirrors. The diode laser frequency itself is stabilized to the Ti:Sapph frequency with a transfer cavity technique. First, we adjust the current to the Toptica laser diode such that both lasers are simultaneously resonant with a TEM_{00} mode of the physics cavity, changing the cavity length if necessary to find a suitable point. We then find a similar resonance overlap for a 25 cm confocal (transfer) cavity into which light from both lasers has been injected, adjusting the length of the transfer cavity as necessary. We use the Ti:Sapph light to lock the transfer cavity length with the Pound-Drever-Hall (PDH) technique [20], a PID controller, and PZT's. Finally, we stabilize the diode laser frequency to the transfer cavity resonance with another PDH signal, derived from FM sidebands at 9 MHz generated by directly modulating the laser diode current.

The rest of the light from the Toptica diode laser is used to generate a PDH signal for stabilizing the length of the physics cavity. Before reaching the cavity, the light goes through an AOM in double-passed configuration and enters a single-mode polarization-maintaining fiber. The AOM allows for scanning the cavity frequency by ± 40 MHz. A monitor photodiode after the fiber output is read by an analog-to-digital sampling card and monitored by a LabVIEW program, which controls the

RF drive power to the AOM in order to maintain the light output from the fiber at a constant power. This is especially important when scanning the cavity frequency, as residual AM sidebands from modulating the diode current give a power-dependent DC offset to the PDH error signal for the physics cavity; this results in a nonlinear scan due to the frequency-dependent AOM diffraction efficiency.

We drive the physics cavity with Ti:Sapph light that passes through a 780 nm single-mode fiber electro-optical modulator (EOSpace) in Mach-Zender configuration to imprint AM sidebands at 150 MHz from the carrier. One sideband is near resonance with the atomic transition and the cavity, becoming the system drive, while the carrier and all other sidebands are reflected from the front cavity mirror. Changing the sideband frequency allows us to probe the frequency response of the cavity-atom system without misalignment of the input laser coupling. Polarization elements (better than 5×10^{-5} extinction) and mode-matching optics prepare the driving laser before it enters the cavity.

Light at 780 nm used for repumping atoms in the MOT is generated from a Sharp laser diode housed in a ThorLabs mount. The laser is slaved to a New Focus Vortex diode laser, which is frequency stabilized to the repumping transition with a Dichroic Absorption Vapor Laser Lock (DAVLL) and PID controller [21]. This system generates about 20 mW of repumper light.

1.3.4 Detection system

A lens at the cavity output collimates the escaping light, and a zero-order half-wave plate (HWP) aligns the polarization to a Wollaston prism, which separates vertically and horizontally polarized light into separate beams. Additional optics allow the choice of sending both beams to the detectors, or of blocking the vertically polarized beam and splitting the horizontally polarized beam between two paths for coincidence measurements. We split off a small fraction of the vertically polarized beam first in order to monitor the intensity of transmitted light at 820 nm; the rest of this light is removed from the signal with 5-nm wide interference filters centered at 780 nm (Semrock MaxLine), such that no detectable level of light at 820 nm reaches the detectors. Passing through spatial filtering optics to remove background light, the signal beams enter a dark box where they are detected by two photomultiplier tube (PMT) units (Hamamatsu R636-10), which measure the average light intensity; or, by remotely activating motorized flip mirrors, to two avalanche photodiode (APD) units (Perkin Elmer SPCM-AQR-12 and -13) for time-resolved photon counting, each with quantum efficiency greater than 50%. The total detection efficiency of light from the cavity is about 30%, as calibrated by an optical power meter and neutral density filters of known attenuation.

The electronic output pulses from the two APDs are first duplicated in a transistor-transistor logic (TTL) voltage divider circuit. One copy of each goes to a counter unit (SR400) for measuring average count rates, or to a nuclear instrumentation module (NIM) logical gate module for coincidence measurements. The

other copy of each goes to a computer time-stamp correlator card (Becker and Hickl DPC-230), which records both channels of TTL events with 164 ps resolution. For measuring photon correlation functions, we record the arrival times of all photons and compute the detector cross-correlation in post-processing with a C++ program, with typical user-defined time resolution of 16.4 ns bins.

Chapter 2

Detecting Single Atoms

2.1 Introduction

Many applications in atomic physics and quantum information hinge on the ability to detect the presence of individual neutral atoms or molecules in order to perform subsequent state manipulation protocols [22, 23]. Optical detection of atoms involves identifying a change in average light intensity due to the presence of the atom. This typically happens by one of two methods: fluorescence detection, in which the atom adds light on top of a background level; or absorption detection, in which the atom removes light from an incident field. Dispersive detection can effectively operate in either of these limits, depending on whether the signal with no atoms is bright or dark. All these techniques require the integration of photon flux until a targeted signal-to-noise ratio is reached; this sets the probability of obtaining a false positive for atom detection.

Fluorescence detection requires high-numerical aperture optics and careful suppression of background light, and generally operates on time scales of tens of milliseconds. The integration time limits the bandwidth with which new atoms can be identified and then manipulated, making this method much better suited for identifying stationary trapped atoms [24, 25, 26]. When detection speed is more important (as when detecting freely moving particles that spend a limited time in

an interaction region), a more useful technique is fluorescence burst detection [27], which looks for above-average count rates over short time intervals [28, 29]. One particularly impressive example [30] showed detection of falling atoms in free space in 60 μs using highly-efficient mirrors and lenses.

In contrast to free-space methods that collect light from as many spatial modes as possible, cavity-based methods limit the optical interactions to one or a few resonant modes, yet give signal-to-noise ratios that may be orders of magnitude larger. Collecting fluorescence in an optical cavity with axis perpendicular to the driving laser gains the benefit of Purcell-enhanced emission [31] into the cavity mode [32, 33, 34]. Experiments based on changes in cavity transmission, which require strong atom-cavity coupling [35], have achieved single atom detection times of 20 μs for moving atoms [7, 32, 36, 37], and as low as 10 μs [34, 38, 39] for trapped atoms. Both methods enable strong suppression of background light through spatial filtering of the output quasimode of the cavity.

We have developed a cavity technique for atom detection that combines elements of driven cavity QED detection and spontaneous emission collection [40]. The technique allows rapid identification of atoms with near maximal coupling to the cavity mode, and their subsequent emission dynamics. This chapter presents our approach, in particular autocorrelation studies of the transmitted light. We identify contributions to the autocorrelation signal from different physical processes, in the short time (atomic decay) and in the long time (transit of atoms through the mode).

2.2 Detection scheme

The basic components of our system are shown in Fig. 2.1. We resonantly drive a TEM_{00} mode of the optical cavity, previously discussed, with a laser sideband tuned to the ^{85}Rb $F = 3$ to $F' = 4$ transition. Intersecting the cavity axis at near-normal incidence is the beam of cold atoms, each of which interacts with the cavity mode for some time before leaving. Because of the large difference in time scales (5 μs transit time through the mode versus 26 ns excited state lifetime), the atoms undergo dozens of spontaneous emission cycles while in the mode volume.

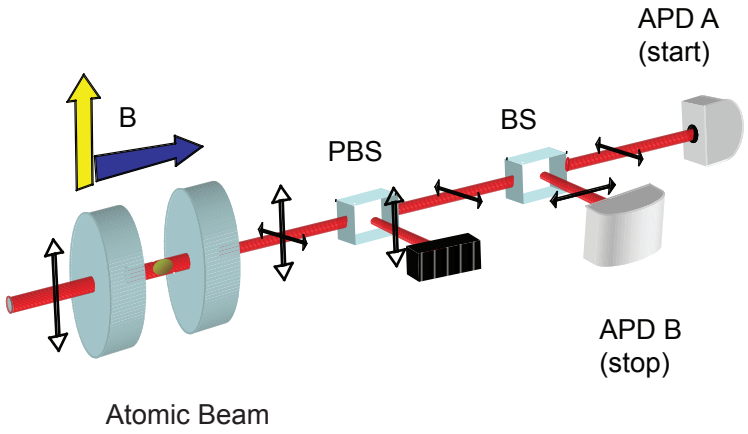

Figure 2.1: Schematic of the apparatus with the basic optical elements necessary for coincidence measurements. Vertically polarized laser light (parallel) drives the high finesse cavity traversed by a continuous beam of cold ^{85}Rb atoms from a magneto-optical trap. The output light passes through a polarizing beam splitter (PBS) that separates the horizontal (perpendicular) polarization, sending it to a nonpolarizing beam splitter (BS) for coincidence measurements using two avalanche photodiodes (APD). The direction of the magnetic field (B) inside the cavity can be parallel to the exciting polarization (yellow arrow, π-polarized drive) or parallel to the direction of light propagation (blue arrow, σ-polarized drive).

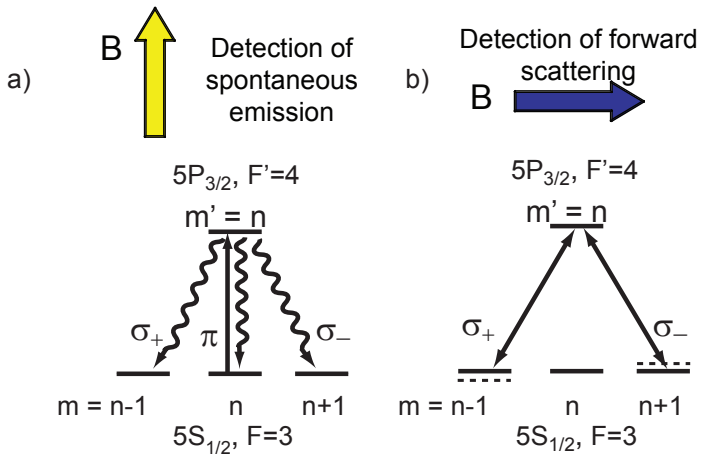

Figure 2.2: a) A linearly polarized driving field excites the atom, but a transition to a ground state level with different m results in emission in the orthogonal polarization. b) Simplified diagram of ^{85}Rb levels relevant to Faraday rotation in an applied magnetic field.

The crux of our detection scheme is the separation of the cavity output field into two distinct polarization components relative to the polarization of the exciting laser: one parallel (driven mode) which is little affected by the transiting atoms (as the cooperativity parameter is relatively small), and the other perpendicular (undriven mode) which in the ideal case is populated only by scattered light from the atoms. This configuration in cavity QED was first used in [41]. As the coupling of the two modes by mirror birefringence is small, the two eigenfrequencies are split by less than 10% of the cavity linewidth, and we can use the two modes for excitation and signal collection, respectively.

We consider two different configurations for excitation. The first has a weak ($<$ 10 G) magnetic field parallel to the incident polarization, forming the quantization axis. The light drives π (Δm=0) transitions in the atoms in this basis

(see Fig. 2.2a). An excited atom can return to its original ground-state m-level through spontaneous or stimulated emission into the parallel (driven) mode; however, there is also some probability to relax into a different m-level through a σ^+ or σ^- ($\Delta m = \pm 1$) spontaneous emission transition, which produces light that is circularly polarized with respect to the magnetic field axis and may be collected by the perpendicular (undriven) cavity mode. Although the cavity coupling strength is modest, the amount of collected light increases measurably from that in free space [10].

The second configuration has a weak magnetic field along the cavity axis, while keeping the same polarization arrangement (see Fig. 2.2b). The linearly polarized drive can then be considered as the sum of two circular components with different indices of refraction due to the Zeeman shift. This results in a Faraday rotation of the drive into the perpendicular mode. Though the single-pass Faraday rotation is small, the high cavity finesse allows the light to compound thousands of rotations before escaping, and the effect becomes appreciable.

A polarizing beam splitter (PBS) sends the two modes to separate detectors, which can resolve individual photon events. From the record of photon detections, we analyze the statistics of emission to look for signs of single atom transits. One advantage of collection into a cavity mode is that we can spatially filter out most sources of background light. However, there are remaining contributions to the perpendicular mode from cavity mirror birefringence and background light that cannot be completely eliminated. The optimal parameters for operation minimize the background influence on the atom detection confidence.

2.3 Theory

To include the effects of Faraday rotation, we consider an atom with one excited state ($m' = 0$) and three ground states ($m = \pm 1, 0$). (See Fig 2.2b). A magnetic field B along the direction of light propagation lifts the ground state degeneracy through the Zeeman effect, resulting in a shift in the dispersion curves and a difference in the phase velocities of the two circular components of light, causing Faraday rotation [42]. We excite the system with vertically polarized light, which is an equal superposition of right- and left-circularly polarized light. The light interacts with the atom and becomes elliptically polarized; the plane of polarization rotates through an angle. The light then passes again through the atom after reflection on the mirror and compounds the rotation. When the light exits the cavity, the total rotation is that of a single pass multiplied by the number of times the light passes through the atom, indicated here by the presence of the cooperativity C (which is proportional to $\mathcal{F}$):

$$\phi = \frac{2g_L\mu_B B/\hbar\gamma_{tot}}{1 + (2g_L\mu_B B/\hbar\gamma_{tot})^2} C, \tag{2.1}$$

where g_L is the Landé factor and μ_B is the Bohr magneton.

The addition of this effect changes Eq. 1.8 (assuming $|\phi| \ll 1$) into:

$$X_\perp = Y\left(2\widetilde{C}_1 C + |\phi|^2\right). \tag{2.2}$$

Equation 2.2 shows that the signal in the perpendicular mode now consists of two parts: a background level of spontaneous emission (which may be considered as $(\sigma^+ - \sigma^-)$ polarization if the drive is $(\sigma^+ + \sigma^-)$, in full analogy to the basis with

π drive), and Faraday-rotated drive which increases from zero to a maximum value of $X_{\perp\text{Faraday}} = YC^2/4$ when $B = \hbar\gamma_{tot}/(2g_L\mu_B)$. For simplicity in what follows we treat the atom-cavity coupling in the basis of π drive.

We analyze the two-time intensity autocorrelation function of the light from the perpendicular mode to understand the dynamics of photon emissions that contribute to the steady-state value of $X_\perp$. We do not distinguish between the two components in Eq. 2.2, treating both as arising from near-resonant scattering of incident light (resonance fluorescence) in which the cavity serves only as a mode in which to collect the light.

For a stream of photons scattered from a single two-level atom undergoing stationary, resonant excitation, the intensity autocorrelation function takes the familiar form for resonance fluorescence antibunching [12]:

$$g_A^{(2)}(\tau) = 1 - e^{-(3\gamma/4)\tau}(\cosh\zeta\tau + \frac{3\gamma}{4\zeta}\sinh\zeta\tau), \tag{2.3}$$

where $\zeta = (\gamma/4)\sqrt{1-8Y}$ is a function of the drive intensity Y. The antibunching referred to here means an increasing slope for increasing times: $dg^{(2)}(\tau)/d\tau|_{\tau>0} > 0$. The condition $g^{(2)}(0) < 1$ indicates that the photons obey sub-Poisson statistics, and is not a necessary condition for the photons to exhibit antibunching [43].

The modification of Eq. 2.3 for the case of an atomic beam passing through a localized excitation region appears in Ref. [44], which adds a number of effects: i., the multiplication of Eq. 2.3 by a window function to include the shape of the mode function encountered by each transiting atom; ii., the scaling of Eq. 2.3 by the inverse of the steady-state mean number of interacting atoms, $\overline{N}$; iii., the addition

of a term $|g_A^{(1)}(\tau)|^2$ to include the beating of fields emitted by different atoms (the Hanbury Brown and Twiss effect [45]); iv., the addition of a constant offset of one arising from uncorrelated emissions from different atoms; and v., the reduction of the correlation factor due to the presence of completely uncorrelated background light. Further generalizations appear in Refs. [46, 47], where the authors also consider the product of the fields that come from atomic emission with a temporally uncorrelated but spatially mode-matched field from background light.

We are able to describe the total correlation function as:

$$g^{(2)}(\tau) = 1 + \frac{1}{(1 + R_b/R_s)^2} \frac{f(\tau) g_A^{(2)}(\tau)}{\overline{N}} + F(\tau; R_b/R_s, \overline{N}) \tag{2.4}$$

where R_b and R_s are the average count rates for background and signal, respectively, and

$$f(\tau) = [\cos(\Omega\tau) e^{-\beta\tau} + 1] e^{-(\tau/T)^2} \tag{2.5}$$

is an empirically-determined window function describing motion of the atom through the cavity mode with Gaussian temporal width T, where a small tilt of the atomic beam with respect to the cavity axis normal results in motion through the standing-wave lobes at frequency Ω. These oscillations decay at a rate β much faster than the transit time, due to the spread in velocities from the atomic source. The function F corresponds to any additional terms related to the beating of signals from different atoms or of signal with background light; since this term represents classical noise sources, it can only contribute light which is bunched around $\tau = 0$ [48]. Any observation of antibunching in our signal must come from the single-atom term $g_A^{(2)}(\tau)$. An explicit observation of F would require a high atom density ($\overline{N} \gg 1$)

since the width is comparable to that of the antibunching signal. (A technique in which the antibunching width was artificially made wider was demonstrated in [49] in order to see this term.)

2.4 Preliminary data analysis

2.4.1 Faraday rotation

The Stokes parameter formalism [50] allows a measurement of the rotation angle ϕ if the amplitudes of the electric field in the two polarizations $\varepsilon_\perp$ and $\varepsilon_\parallel$ are known:

$$|\phi| = \frac{|\varepsilon_\parallel \varepsilon_\perp|}{|\varepsilon_\parallel|^2 - |\varepsilon_\perp|^2} \approx \left|\frac{\varepsilon_\perp}{\varepsilon_\parallel}\right|, \tag{2.6}$$

where the approximation is made for $|\varepsilon_\parallel| \gg |\varepsilon_\perp|$. We measure the count rates in the perpendicular mode as a function of applied magnetic field along the cavity axis to determine the location of maximum Faraday rotation. For the measurements in this chapter we do not optically pump the atoms to $m = 0$ before they enter the cavity. The peak rotation is different depending on the sign of the magnetic field, probably due to an asymmetry in the population distribution. We obtain a maximum of $|\phi| = 0.035 \pm 0.007$ rad from the measured increase in the count rate with a field magnitude of 3.3 Gauss (calibrated from Zeeman shifts in absorption.) To make explicit the effects of the cavity, we estimate the effective number of maximally-coupled atoms by using Eq. 1.7 and measuring the driven mode transmission. This was greater than 0.95, giving a bound of C <0.01 or $\overline{N}$ <0.1 effective maximally-

coupled atoms (for π transitions from $m = 0$). Calculating the free-space absorption length for 0.1 atoms and our cavity waist, we would expect a maximum rotation of the order of 3 μrad [42]. The enhancement by a factor of approximately 10,000 is a result of the cavity finesse.

2.4.2 Photons per atom

The formula of Mandel relates the photon number distribution $P(n)$ with the atom number distribution $P_{atom}(m)$:

$$P(n) = \sum_m P(n|m) P_{atom}(m), \tag{2.7}$$

where $P(n|m) = (\alpha m)^n \exp(-\alpha m)/n!$ is the conditional probability of detecting n photons when there are m atoms in the cavity volume, each contributing a mean of α photons to the signal with a Poisson distribution of number [51]. This shows that the super-Poisson fluctuations of the light arise from the combined Poisson fluctuations in atom number and photons scattered, with α an extractable parameter.

We follow the method of Ref. [32] to relate the mean and mean-squared photon number ($\langle n \rangle$, $\langle n^2 \rangle$) to α:

$$\frac{\langle n^2 \rangle}{\langle n \rangle} - 1 = \langle n \rangle g_{aa} + \alpha, \tag{2.8}$$

where the atom-atom correlation function is $g_{aa} = \left(\langle m^2 \rangle - \langle m \rangle\right) / \langle m \rangle^2$, which for Poisson atomic fluctuations reduces to $g_{aa} = 1$.

Figure 2.3 shows a detail of the plot of the experimental values for the left side of equation (2.8) with the two different detection methods: Faraday rotation on the

top and no Faraday rotation on the bottom. We calculate the statistics based on 300 s time series of photon detections that we divide into a series of time bins of equal width. Longer bin sizes have a larger average number of counts (horizontal axis). The intercept gives the value of α. A linear fit for bins from 50 μs to 100 μs ($\langle n \rangle = 1.81$ to 3.63, off the scale of the plot in Fig. 2.3) in the Faraday case gives a vertical axis intercept of $\alpha = 0.196 \pm 0.003$ photons detected per atom, and a slope of 1.033 ± 0.001. The intercept in the no Faraday case (for a fit from $\langle n \rangle = 0.50$ to 1.00) is $\alpha = 0.036 \pm 0.002$ photons detected per atom and a slope of 1.026 ± 0.003. The drive in both cases is two photons. The values of the slopes indicate that the assumption of Poisson statistics for the atom number is well justified.

Figure 2.4 shows the extracted values of α as a function of cavity photon number (driving intensity) spanning more than two orders of magnitude. There are data points (rhombs) that come from Faraday rotation and one with spontaneous emission alone (circles). The latter is smaller by almost a factor of five. α increases linearly with drive until atomic saturation intensity ($n_{\mathrm{sat}} = 5.3$ photons for the $m = 0$ to $m' = 0$ transition), where in addition to saturation of the scattering rate, optical pumping effects also start to enter. Each point on Fig. 2.4 comes from a least-squares fit similar to those in Fig. 2.3. The count rates in the perpendicular mode and the values of α give an atomic flux through the mode of approximately 160,000 atoms s^{-1}. (The flux is set much smaller than the maximum available in order to isolate primarily single-atom events.)

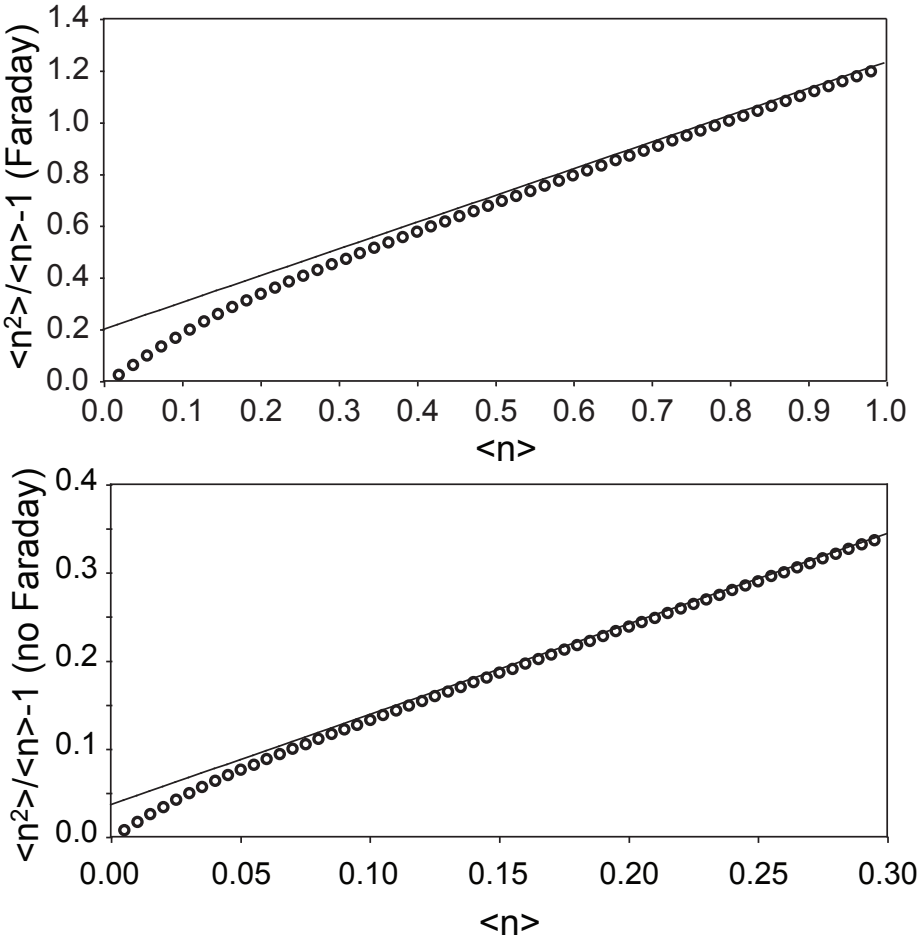

Figure 2.3: Examples of data (circles) and least-squares fits (continuous line) to Eq. (2.8) in the large-$\langle n \rangle$ region for Faraday rotation (top) and for no Faraday rotation (bottom) in the cavity as a function of average number of photons in a time bin ($\langle n \rangle$).

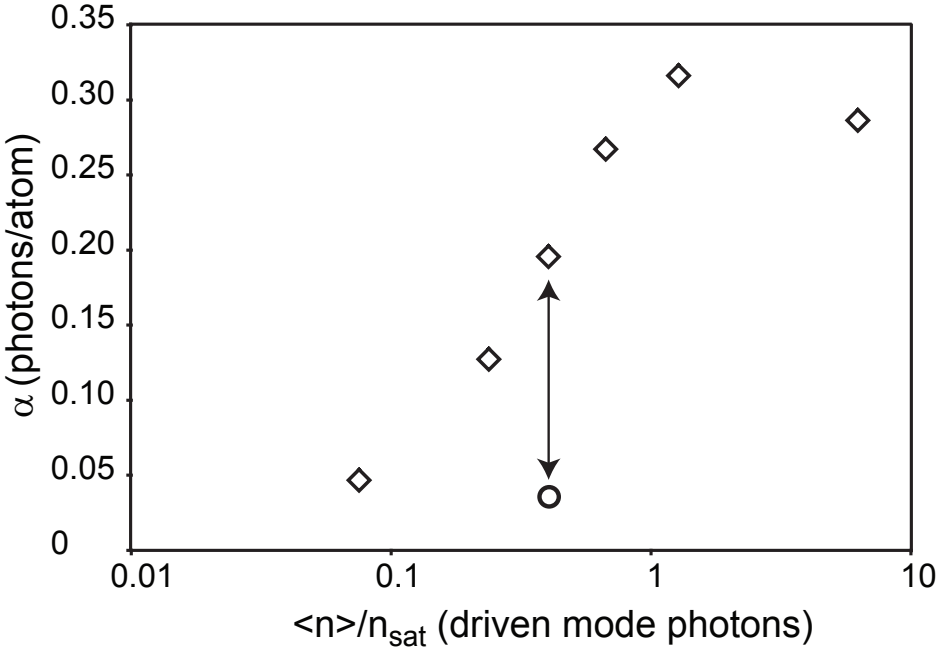

Figure 2.4: Counts detected from a single atom (rhombs for Faraday, circle for non Faraday) as a function of intensity of the exciting laser normalized by the saturation photon number. The arrows indicate the points extracted from the plots of Fig. 2.3. The statistical error bars are smaller than the size of the data points.

2.5 Analysis and optimization of detection

Three identifiable sources of background counts contribute to the measurement of the perpendicular mode: intrinsic detector dark counts (approximately 300 s^{-1} each), scattered light from the MOT beams (approximately 2000 s^{-1}), and the birefringence of the cavity (less than 5×10^{-5} of the driven mode count rate). The light from the MOT dominates the background count rate at low driving intensity; however, at higher intensity, light from cavity birefringence is the main contributor to the degradation of the signal-to-background ratio. A single photon escaping in the perpendicular mode most likely comes from an atom in the cavity; however, there is at best still a 4% probability that it comes from background counts. We suppress the probability of a false atom detection by requiring photon coincidences in a time window smaller than the transit time of an atom across the cavity mode [7]. We have implemented this in real time for preliminary measurements using a NIM electronic coincidence module. The first perpendicularly polarized photon detection ("start") opens a gate of variable width which allows counting pulses from the "stop" APD. Detection of one or more of these yields an atom detection event.

Figure 2.5 shows the signal-to-background ratio calculated from photon time series for the rate of single photon detection (open rhombs), two-photon coincidence (open squares), and three-or-more-photon coincidence events (open triangles) in a 1 μs window as a function of driving intensity. The maximum occurs at the same driving intensity for all three. Two photons within a 1 μs window improves the signal-to-background ratio by more than an order of magnitude compared to de-

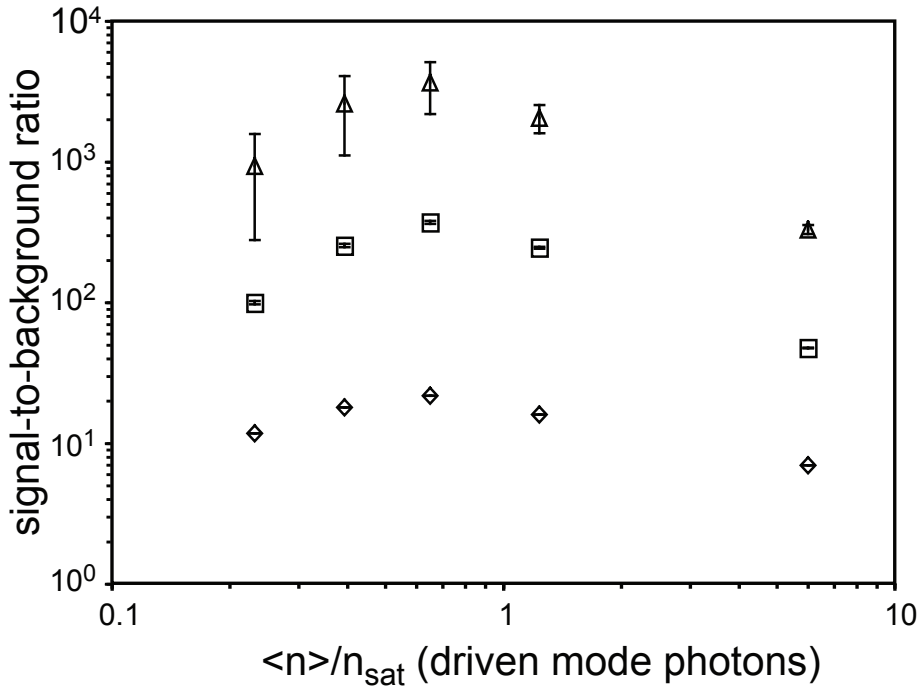

Figure 2.5: Signal-to-background ratio as a function of normalized driving laser intensity for single detection (open rhombs), double coincidence detection (open squares), and triple coincidence detection (open triangles) in a 1 μs window with Faraday rotation of the drive.

tection of single photons. The three-photon coincidence gives a better ratio but significantly decreases the rate of detection as evident in the error bars associated with each point. The three sets achieve their maxima just before the atomic saturation intensity, due to background counts from cavity birefringence that continue to increase linearly with drive. The contribution to the coincidences from detector afterpulsing is small (less than 1%) and does not affect the results.

To evaluate the probability of making a false detection for various coincidence gate times, we extract the fidelity of detection F versus gate length for two-photon coincidence based on the time record. We calculate the waiting time distribution

of photon arrivals on a single APD by making a histogram of the time separation between consecutive detections. The integral of the waiting time distribution gives the number of two-photon coincidences c in a given time window. We calculate c with and without atomic flux to obtain:

$$F = 1 - c_{without}/c_{with}. \tag{2.9}$$

The fidelity (one minus the probability of error) reaches more than 99% at 0.1 μs, and 99.7% at 1 μs with Faraday rotation, but only 96.7% at 1 μs with detection of spontaneous emission alone. The fidelity decreases at longer times. The fidelity is optimal for times between 1 and 5 μs, determined by the distribution of atom transit times.

2.6 Intensity autocorrelation

We ensure that our coincidence detection scheme is sensitive to single atoms by measuring the intensity autocorrelation function ($g^{(2)}(\tau)$) of the perpendicular mode under very weak driving intensity at the same atomic beam density used during detection measurements. If we consider the light in the perpendicular mode as coming from resonance fluorescence, the antibunching can only arise from photon pairs from the same atom. The observation of antibunching in our signal is strong indication of our ability to detect photon coincidences from a single atom in less than 1 μs.

Figure 2.6 shows two examples of an autocorrelation function around $\tau = 0$ with and without Faraday rotation for the same driving intensity (0.4 $n_{\rm sat}$). The

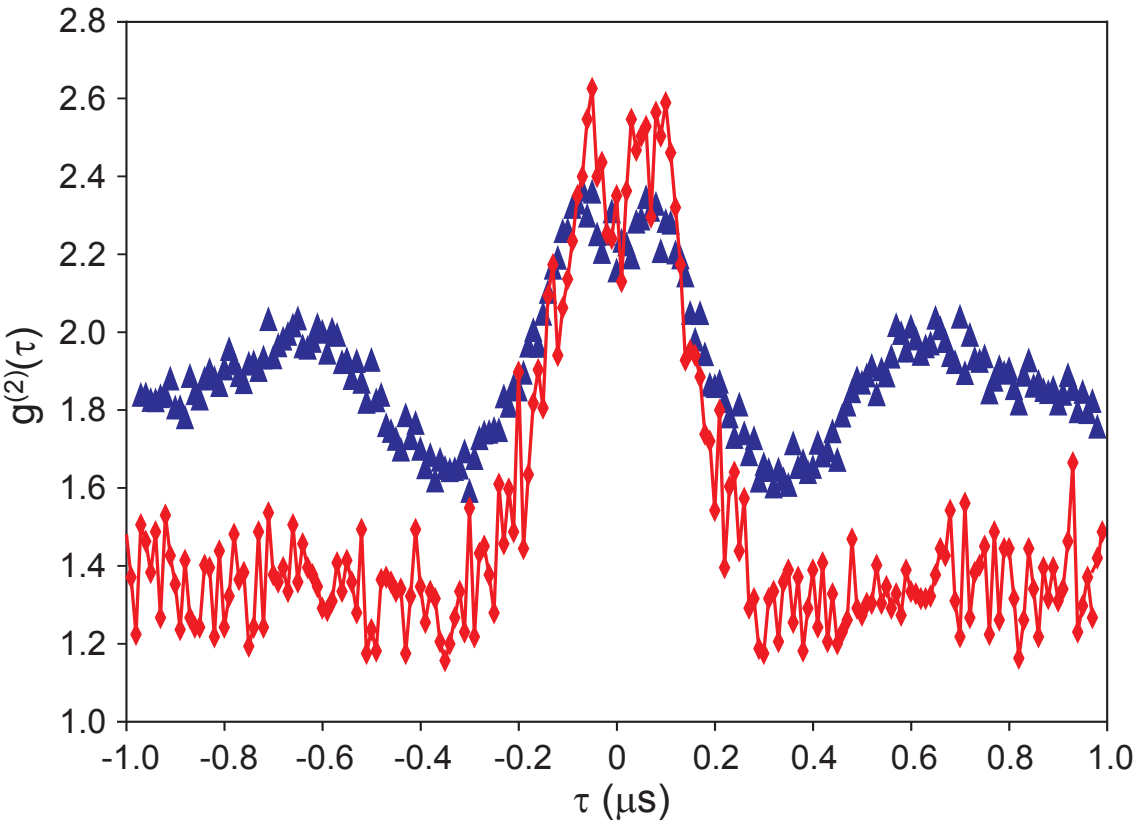

Figure 2.6: Intensity autocorrelation function ($g^{(2)}(\tau)$) of the perpendicular mode with (triangles) and without (diamonds) Faraday rotation, at a driving intensity of 0.4 n_{sat}.

antibunching is visible and lasts for a time of the order of the excited state lifetime (26 ns). The area under the curve is larger with Faraday rotation, indicating a substantial increase in photon flux from individual atoms. The antibunching is less pronounced without the rotation because of the lower signal-to-noise ratio.

Since we record the photon detections as continuous time series, we can also look at the long-term behavior of the autocorrelation in the context of resonance fluorescence as presented in Ref. [44, 46, 47]. We fit the data to Eq. 2.4 with free parameters $\overline{N}$, T, β, and Ω, excluding the term $F(\tau)$ and the region $|\tau|$ <50 ns

where it is important. We find excellent agreement in this outer region (reduced χ^2=1.03 for points out to ± 5 μs). Fig. 2.7 shows the fit to the data taken at a driving intensity of 0.24 $n_{\rm sat}$. The damped oscillation at Ω=1.5 MHz corresponds to motion through the standing wave with a period of 0.67 μs (a velocity of 0.58 m/s along the cavity axis) and a damping time of $1/\beta$=0.29 μs. Monte Carlo simulations of the transit show good agreement with this damping time based on the geometric collimation of transverse velocities from the source [19]. The Gaussian background gives a mean atom number of $\overline{N}$=0.88, and a $1/e$ waist of T=2.7 μs (a mean velocity of 20.7 m/s across the Gaussian mode). The ratio of the velocities gives a beam tilt of 1.6° with respect to the cavity axis normal. Although we take care to align the cavity under the exit hole of the atomic source, the cavity mode is not necessarily centered on the two mirrors, and the transverse beam width allows for small inclinations of the beam.

The full structure of the correlation function depends not only on the above parameters (properties of the atomic beam), but also on the intensity of the drive, which can change the atomic response or increase the amount of background light from cavity birefringence. Fig. 2.8 shows the evolution of the autocorrelation function as the driving intensity increases by two orders of magnitude. We observe a transition from antibunching to bunching with higher drive. The behavior comes from the term $F(\tau)$ in Eq. 2.4 which includes beating of the birefringence light with the atomic emissions. This is in contrast to the transition seen in Ref. [49], where the atomic density is increased such that the constant $|g_A^{(1)}(\tau)|^2$ term (part of our $F(\tau)$) becomes visible. In separate experiments at low intensity we have also

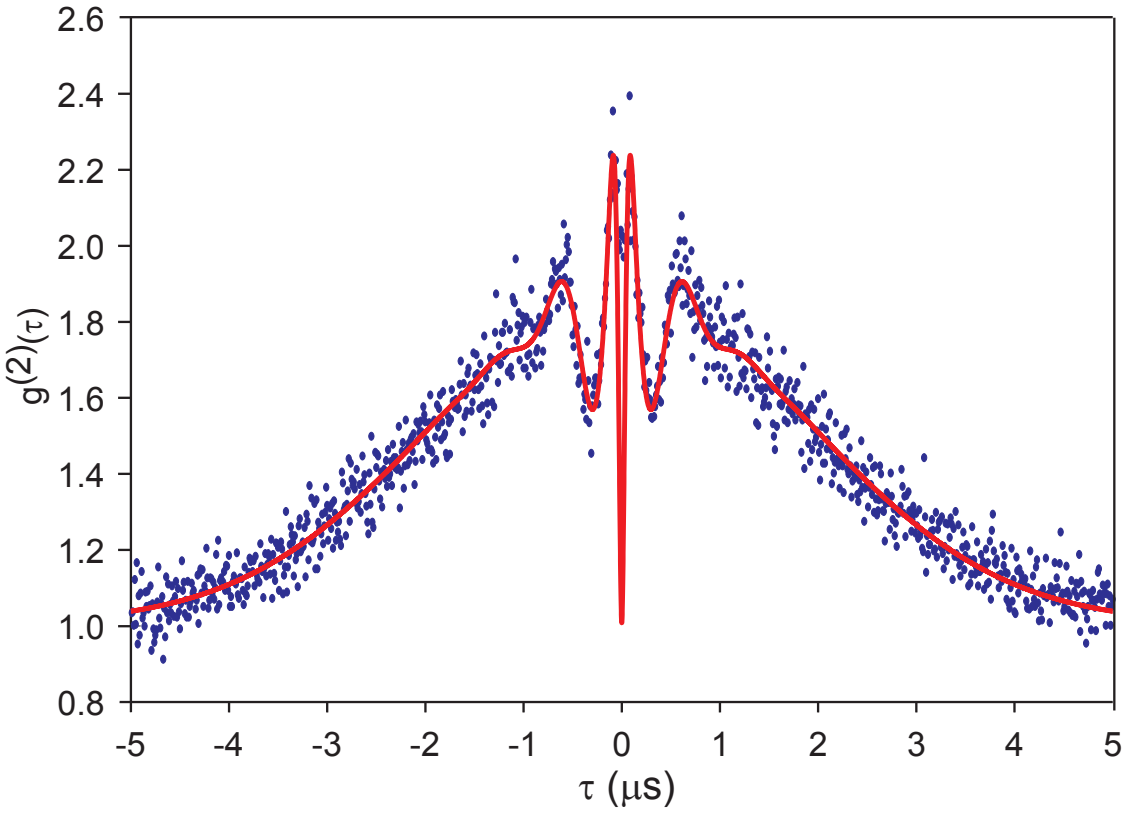

Figure 2.7: Intensity autocorrelation function ($g^{(2)}(\tau)$) of the perpendicular mode at 0.24 $n_{\rm sat}$. The continuous line is the theoretical fit to Eq. 2.4.

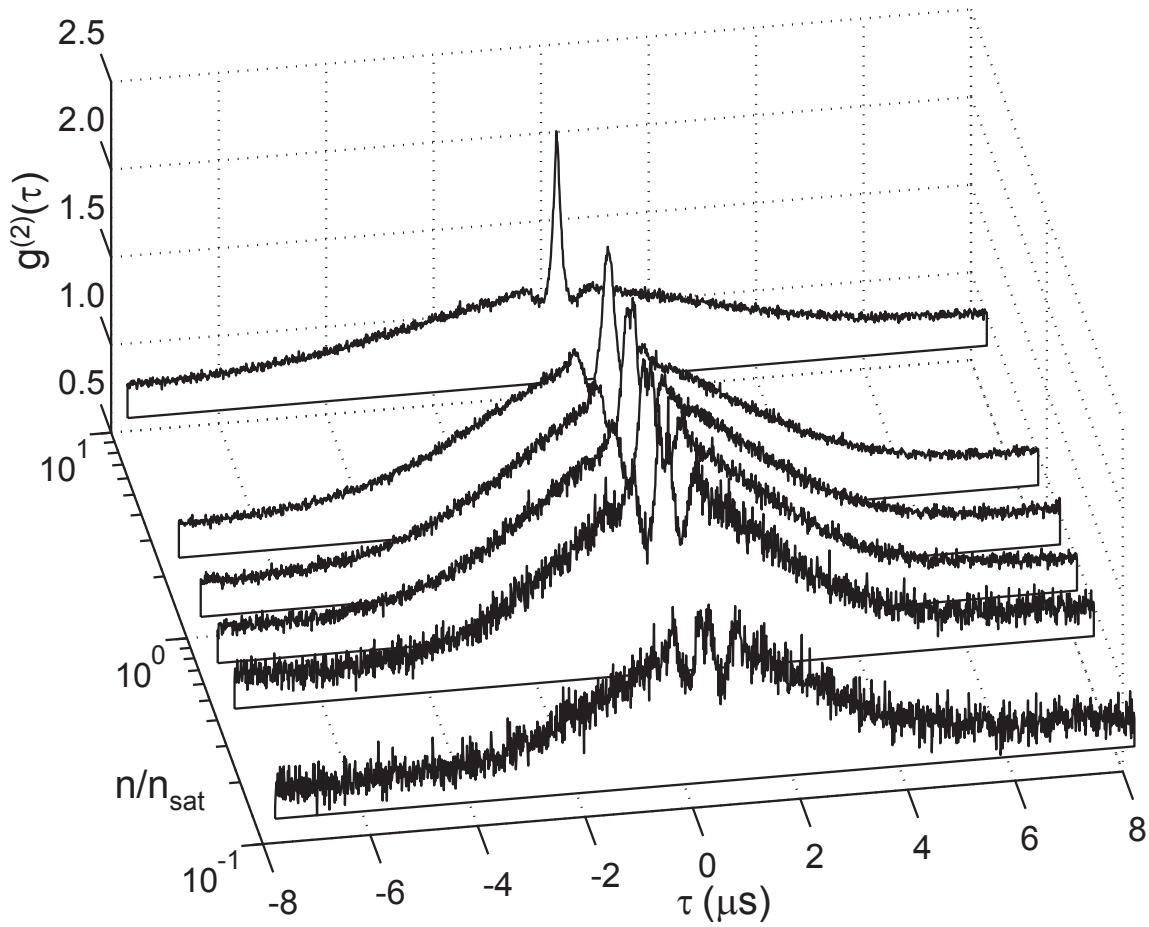

Figure 2.8: Intensity autocorrelation function ($g^{(2)}(\tau)$) of the perpendicular mode for different values of photon number (intensity) in the driven mode.

followed the disappearance of the antibunching as we increase the number of atoms.

Even when the actual density of atoms is kept constant, the effective excitation volume and thus the value of $\overline{N}$ increases with power, as atoms near the nodes and wings of the mode start to interact [52]. This process reaches a maximum above saturation intensity, when the only unsaturated atoms are too weakly coupled to emit into the mode. Fig. 2.9a. shows the extracted values of $\overline{N}$ versus driving

intensity for the autocorrelations in Fig. 2.8. The line shows the expected shape of the saturation, assuming that the probability of collecting a photon from an atom is proportional to the product of a constant $g^2(x,y,z)$ for collection and a saturating strength of excitation ($[(n/n_{\rm sat})g^2(x,y,z)]/[1+(n/n_{\rm sat})g^2(x,y,z)]$), which is consistent with the expression $Y2\widetilde{C}_1C$ in Eq. 1.8, modified for strong driving. We obtain the theoretical line by integrating this product over a volume much larger than the cavity mode, and using a least-squares fit to scale the vertical axis and $n_{\rm sat}$.

Using the extracted parameters of mean atom number and mean transit time from the two-APD correlation measurements, together with the extracted values of α from the one-APD measurements, we can predict the expected macroscopic count rates as $R_s = \overline{N}\alpha/2T$. Fig. 2.9b shows that we obtain excellent agreement for low intensities, while the highest intensity drive (largest birefringence background) disagrees significantly. This comes from the large contribution from the beating between background and signal, which generates the large central peak in the measured autocorrelation.

We emphasize that although the mean number of interacting atoms is approximately one, this is not the same as the effective number of maximally-coupled atoms, since most are weakly coupled. To explore this numerically, we use the work of Carmichael and Sanders [53]. We distribute atoms randomly and uniformly across the cavity mode function such that the mean density is 0.88 atoms within two mode waists (similar to the measured value for low driving intensity). Allowing the atom number to fluctuate with a Poisson distribution, we sum the individual coupling

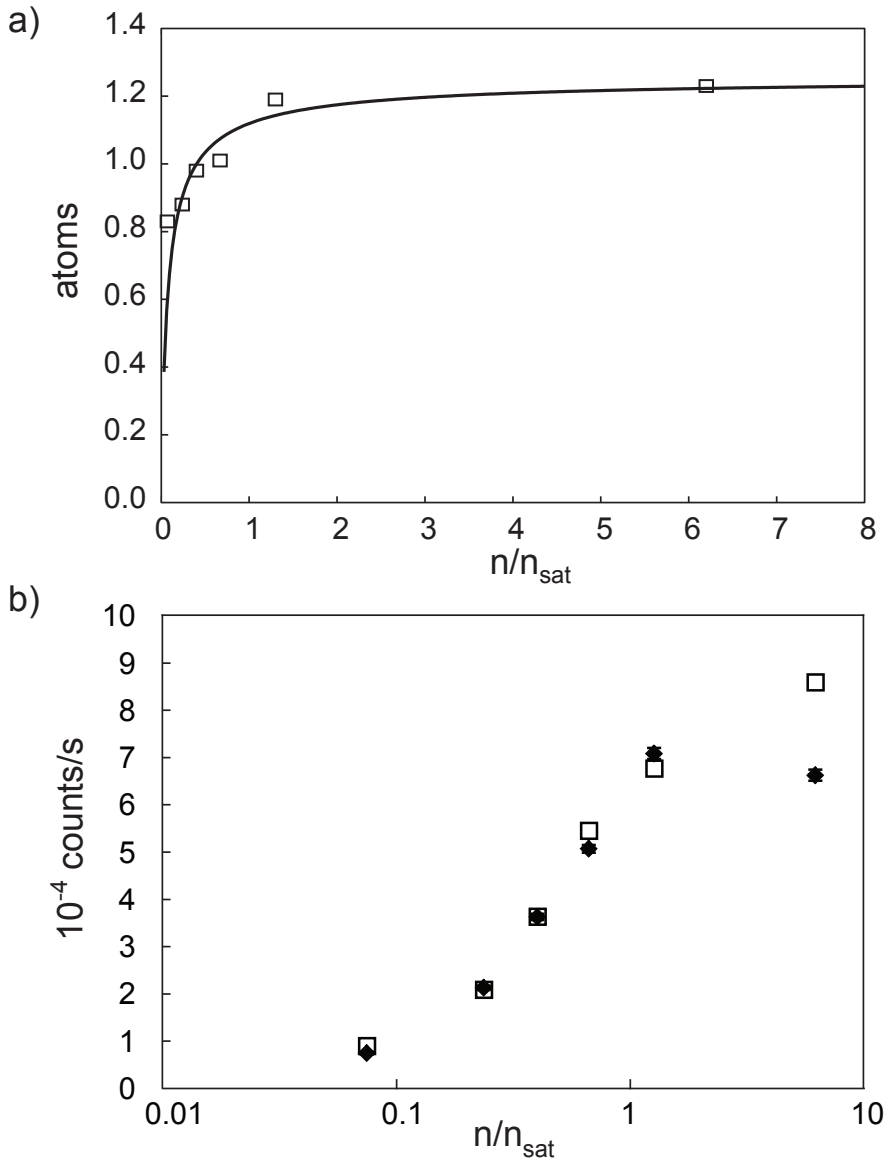

Figure 2.9: a) Measured mean number of interacting atoms, and theory curve showing the expected saturation. b) Measured (filled rhombs) count rates in the perpendicular mode together with those predicted (open squares) from the extracted mean number of atoms, photons per atom, and transit time.

strengths for each configuration of atoms and weight by the atomic number distribution to obtain the mean steady-state effective number of atoms, which in this case is 0.04. Using the mean value of C_1=0.09 for π transitions from the ground state, this gives a driven mode transmission of approximately 0.99 from Eq. 1.7, consistent with the experimental conditions for single atom detection. A rapid decrease in probability above one effective atom indicates that we operate in a density regime of single-atom coupling, with a low probability of having two atoms simultaneously coupled by more than half of the maximum value. This numerical result together with the antibunching in the perpendicular mode counts confirms that the measured signals indeed arise primarily from single-atom emission bursts.

Chapter 3

Ground-State Quantum Beats

3.1 Introduction

Quantum beats are oscillations in the radiation intensity of an ensemble of excited atoms due to interfering emission pathways. They must be counted amongst the earliest predictions of quantum mechanics [54]. So-called "Type-I" atoms exhibit beats at the separation frequency of two excited states which, prepared in a superposition, decay to a common ground state. The preparation may be achieved in a number of ways, e.g., through pulsed optical excitation [55, 56] or cascade emission [57]. In all cases the coherence lasts for the excited state lifetime, unlike ground-state coherence, which can last long enough to be interrogated later and, for this reason, is favored by the field of quantum information.

We consider an unusual situation where *ground*-state coherence gives rise to a long-lived quantum beat in spontaneous emission [58]. As repeatedly noted [54, 59, 60], QED predicts no beat in the decay of a "Type-II" atom to non-degenerate ground states, since they are orthogonal. Nevertheless, while beats may be absent from the mean intensity, they can still lie hidden in the fluctuations. In an elegant experiment in the 1950's, Forrester *et al.* [61] showed this for the (classical) beating of light from a pair of incoherent sources. We proceed in similar spirit; we recover a long-lived quantum beat from fluctuations.

In contrast to recent experiments [62, 63], which aim for deterministic quantum control, the ground-state coherence in our experiment is both prepared and read out by spontaneous emission. Moreover, our measured beat is different from that seen by Schubert *et al.* [64], where an interference occurs in absorption rather than emission.

Creation of coherence through spontaneous emission, so-called spontaneously generated coherence, has been discussed in the theoretical literature [65, 66, 67] and indirect experimental evidence reported for spontaneous creation of electron spin coherence in charged GaAs quantum dots [68]. We detect only spontaneous emission, and therefore make a direct and unambiguous observation of spontaneously generated coherence. We realize, in a continuously driven variation, the scheme of Zajonc [69] for generating ground-state quantum beats on the principle of the quantum eraser [70].

3.2 Theoretical model

Beginning with an outline of the scheme, we consider first one idealized atom then a realistic atomic ensemble. Consider an atom with Zeeman structure in its ground and excited states (Fig. 3.1a) interacting with degenerate, orthogonally polarized cavity modes, H and V; a weak magnetic field sets the quantization axis in the V direction, and mode V is weakly and continuously driven (Fig. 3.1b). The atom is prepared in state $|g_0\rangle$ from which it is excited to $|e_0\rangle$ by the V mode (Fig. 3.2A). It may return to the ground state emitting a π, σ^+ or σ^- photon, or

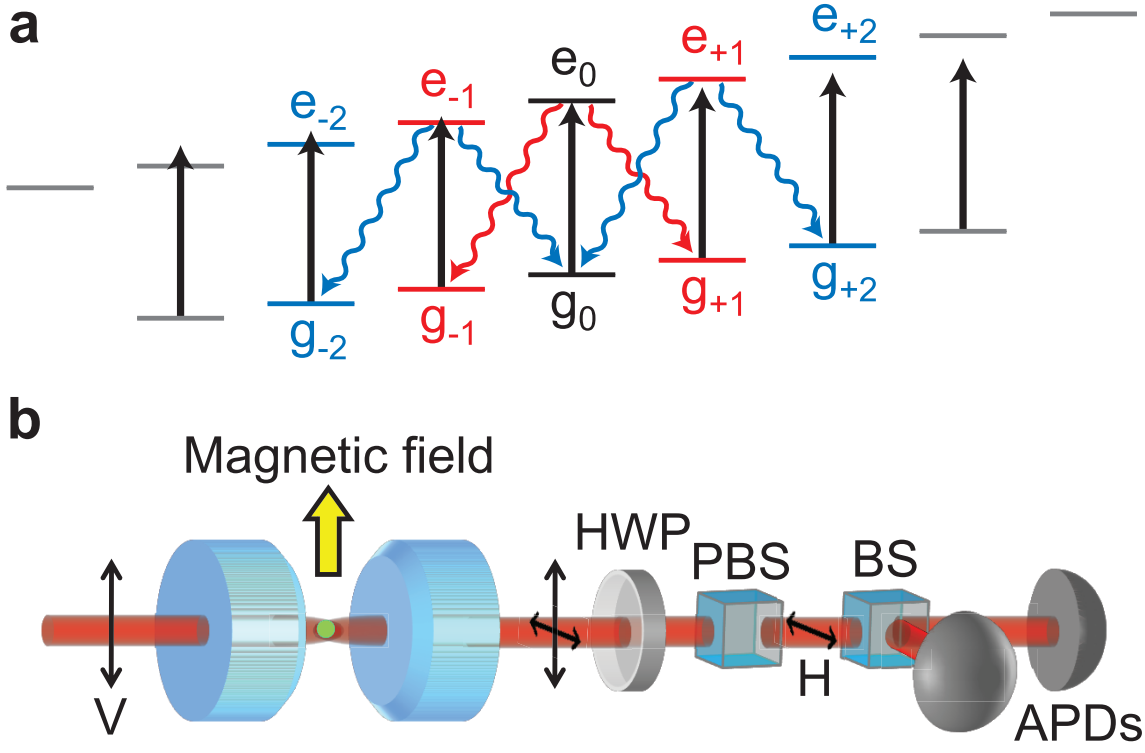

Figure 3.1: Experimental system for observation of ground-state quantum beats. (a) π-excitation of an $F = 3$ to $F' = 4$ transition with scattering of a first (red) and second (blue) photon into the H mode; b) schematic of the apparatus, HWP: half-wave plate, PBS: polarizing beam-splitter, BS: beam-splitter, APD: avalanche photodiode.

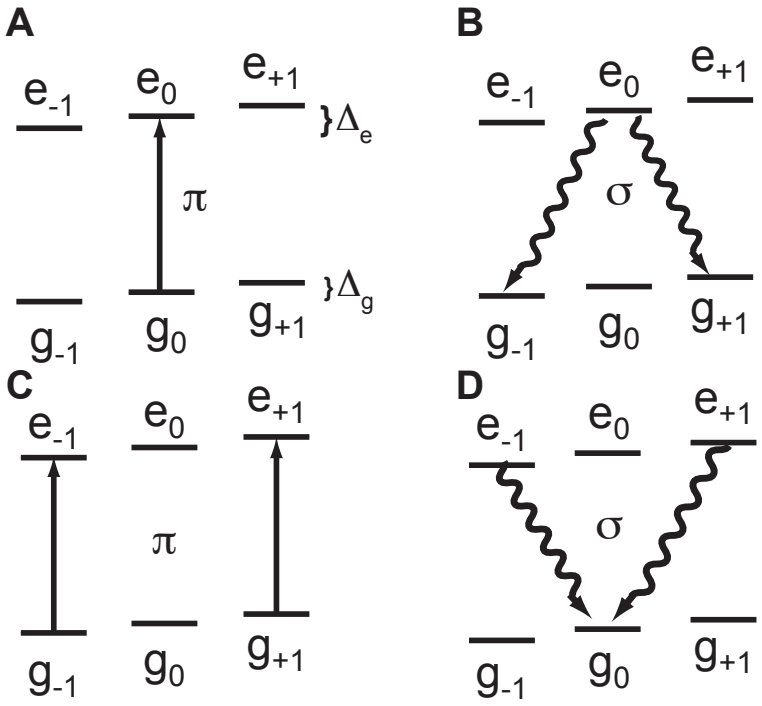

Figure 3.2: Simplified model of quantum eraser process. A) π excitation from g_0 to e_0; (B) Spontaneous decay by σ transitions to superposition of g_{-1} and g_{+1}; (C) π excitation to superposition of e_{-1} and e_{+1}; (D) Spontaneous decay by σ transitions back to g_0.

any linear combination conserving angular momentum. In the given geometry, only σ^+ or σ^- light couples to the H mode, with the helicity undetermined; thus, if the emitted photon escapes the cavity before being reabsorbed, its detection places the atom in the superposition $|\psi'\rangle = |g_{-1}\rangle + |g_{+1}\rangle$ (Fig. 3.2B). The atom is now in the ground state with angular momentum perpendicular to the magnetic field, and thus performs Larmor precession. When subsequently reexcited by the driven V mode, state

$$|\psi'\rangle = e^{i\phi(\tau)}|e_{-1}\rangle + e^{-i\phi(\tau)}|e_{+1}\rangle \tag{3.1}$$

is reached, with phase $\pm\phi(\tau)$ gained through its precession in the ground state (Fig. 3.2C). From here the atom can decay back to $|g_0\rangle$, emitting a second H-mode photon (Fig. 3.2D). The probability to do so depends on $\phi(t)$, giving rise to quantum beats.

In summary, there are two paths for scattering a pair of photons into the H mode: $|g_0\rangle \to |e_0\rangle \to |g_{+1}\rangle \to |e_{+1}\rangle \to |g_0\rangle$ and $|g_0\rangle \to |e_0\rangle \to |g_{-1}\rangle \to |e_{-1}\rangle \to |g_0\rangle$. The phase gained from the ground-state Zeeman shift (precession) differs along the two paths, which interfere to produce oscillations in the rate of delayed coincidences—*i.e.*, in the correlation function $g^{(2)}(\tau)$. Note that after the first photon is detected "which path" information is available, since $|g_{+1}\rangle$ and $|g_{-1}\rangle$ are distinguishable in principle. This information is erased by the second detection.

What we have presented is a single-atom idealization. It neglects the presence of more than one atom in the cavity (not admissible for an atomic beam), spontaneous emission to non-cavity modes, the finite cavity decay rate, and the full

complement of magnetic sublevels for the employed $F = 3$ to $F' = 4$ transition (Fig. 3.1a). These features are included in a full quantum trajectory treatment, including a Monte Carlo simulation of an atomic beam [71]. Two approximations are adopted: (i) the driven mode is treated semiclassically (with absorption still taken into account), and (ii) reabsorption of H-mode photons is neglected. The approximations are justified by our moderate dipole coupling strength.

Consider first an atom prepared in $|g_0\rangle$ that has not yet suffered a spontaneous emission. Let $|a_i\rangle$, $|a_i'\rangle$, and $|a_i''\rangle$ denote unnormalized states expanded, respectively, over the $m_i = 0$, $m_i = \pm 1$, and $m_i = 0, \pm 2$ sub-manifolds, as indicated by the black, red, and black plus blue levels of Fig. 3.1a. These states correlate with the scattering of zero, one, and two photons into the H mode. Should the atom undergo a spontaneous emission (to non-cavity modes), the expansion manifolds, after the quantum jump, are unchanged for a π-emission but move one step to the right or left for a σ-emission ($m_i \to m_i \pm 1$). Keeping track of these shifts, the system state is expanded as

$$\begin{aligned} |\psi\rangle &= |0\rangle|A\rangle + |1\rangle\left(\sum_{i=1}^{N} |a_i'\rangle|A\rangle_i\right) \\ &\quad + \sqrt{2}|2\rangle \sum_{i=1}^{N}\left(\frac{1}{2}\sum_{j\neq i=1}^{N} |a_i'\rangle|a_j'\rangle|A\rangle_{ij} + |a_i''\rangle|A\rangle_i\right), \end{aligned}$$

where $|0\rangle$, $|1\rangle$, and $|2\rangle$ denote zero, one, and two photons in the H mode, N is the (time-varying) number of interacting atoms, $|A\rangle = |a_1\rangle|a_2\rangle \ldots |a_N\rangle$, $|A\rangle_i$ is the state $|A\rangle$ with $|a_i\rangle$ omitted from the product, and $|A\rangle_{ij}$ is the state $|A\rangle$ with $|a_i\rangle$ and $|a_j\rangle$ omitted from the product. This base state evolves under the coherent drive and coupling to the H mode, the coming and going of atoms as they transit the

cavity, and spontaneous emission. From it, at regular sample times, we initiate the collapsed state $|\psi'\rangle = \hat{b}|\psi\rangle$, where $\hat{b}$ annihilates an H-mode photon; thus, the ground-state coherence is prepared as an entangled state of N atoms, which then evolves in parallel with $|\psi\rangle$:

$$\begin{aligned} |\psi'\rangle &= |0\rangle \sum_{i=1}^{N_0} |b_i'\rangle |A\rangle_i \\ &\quad + |1\rangle \sum_{i=1}^{N_0} \left(\sum_{j\neq i=1}^{N} |a_j'\rangle |b_i'\rangle |A\rangle_{ij} + |b_i''\rangle |A\rangle_i \right), \end{aligned} \tag{3.2}$$

where $|b_i'\rangle = |a_i'\rangle$ and $|b_i''\rangle = 2|a_i''\rangle$ at the start of a sample, after which $|b_i'\rangle$ ($|b_i''\rangle$) and $|a_i'\rangle$ ($2|a_i''\rangle$) differ due to their correlation with zero (one) rather than one (two) H-mode photons; $N_0 \leq N$ is the number of surviving entangled atoms, *i.e.*, those remaining in the cavity.

The source of the quantum beat is the atomic ground-state coherence preserved in the vacuum of the cavity, i.e., the first term in Eq. (3.2). The *system* ground state—both atoms and cavity—does not decay, and through π-excitation drives a sustained excited-state oscillation in the atom mirroring Eq. (3.1):

$$\frac{g_{m_i-1} e^{i\delta_g \tau}}{\gamma - i(m_i - 1)\Delta} |e_{m_i-1}\rangle + \frac{g_{m_i+1} e^{-i\delta_g \tau}}{\gamma + i(m_i + 1)\Delta} |e_{m_i+1}\rangle, \tag{3.3}$$

with $\Delta = \delta_e - \delta_g$, where δ_g (δ_e) are ground-state (excited-state) Zeeman detunings, $g_{m_i \pm 1}$ are Clebsch-Gordan coefficients, and γ is the excited state linewidth; m_i tracks the state reached by atom i through possible spontaneous emissions. From Eq. (3.3), oscillation at the *ground*-state frequency $\pm\delta_g$ is passed to the probability amplitudes for emitting a second H-mode photon through $|b_i''\rangle$ and $|a_j'\rangle|b_i'\rangle$ in Eq. (3.2); note that $|b_i'\rangle$ is a source term driving the equation of motion for $|b_i''\rangle$ (the blue wavy lines

plus π-excitation in Fig. 3.1a). Only the amplitude and phase, but not the frequency of the oscillation, will be affected by a detuning of the drive from the atom.

The probability for emitting a second H-mode photon contains a term proportional to $\langle b_i''|b_i''\rangle$, summed over all surviving entangled atoms. It accounts for the scattering of a first and second photon by the same atom and shows the quantum beat introduced above. There is also a term computed from the norm of $|a_j'\rangle|b_i'\rangle + |a_i'\rangle|b_j'\rangle$, $i \neq j$, which adds probability amplitudes for "a first photon from atom i and a second from atom j," and "a first photon from atom j and a second from atom i." If the scattered fields were classical, $\mathcal{E}_i^b$ at time t and $\mathcal{E}_i^a$ at time $t+\tau$, one would have the intensity $|\mathcal{E}_j^a\mathcal{E}_i^b + \mathcal{E}_i^a\mathcal{E}_j^b|^2$, where the interference $2\mathrm{Re}(\mathcal{E}_j^{a*}\mathcal{E}_j^b\mathcal{E}_i^{b*}\mathcal{E}_i^a)$ disallows assignment of the first detection (superscript b) to the intensity of either source (similarly the second). An assignment may be made in principle, however, since one and only one atom changes its ground state when the photon is detected. The change could be seen if one looked, thus providing "which-path" information. As we do not look, the two quantum paths, "atom i then j" and "atom j then i", interfere—after a second detection both atoms have changed state, so the "which-path" information is erased. This interference also creates a quantum beat, as a term analogous to the Hanbury Brown and Twiss thermal bunching peak [45], or to the beating of light from independent atoms observed in Ref. [61].

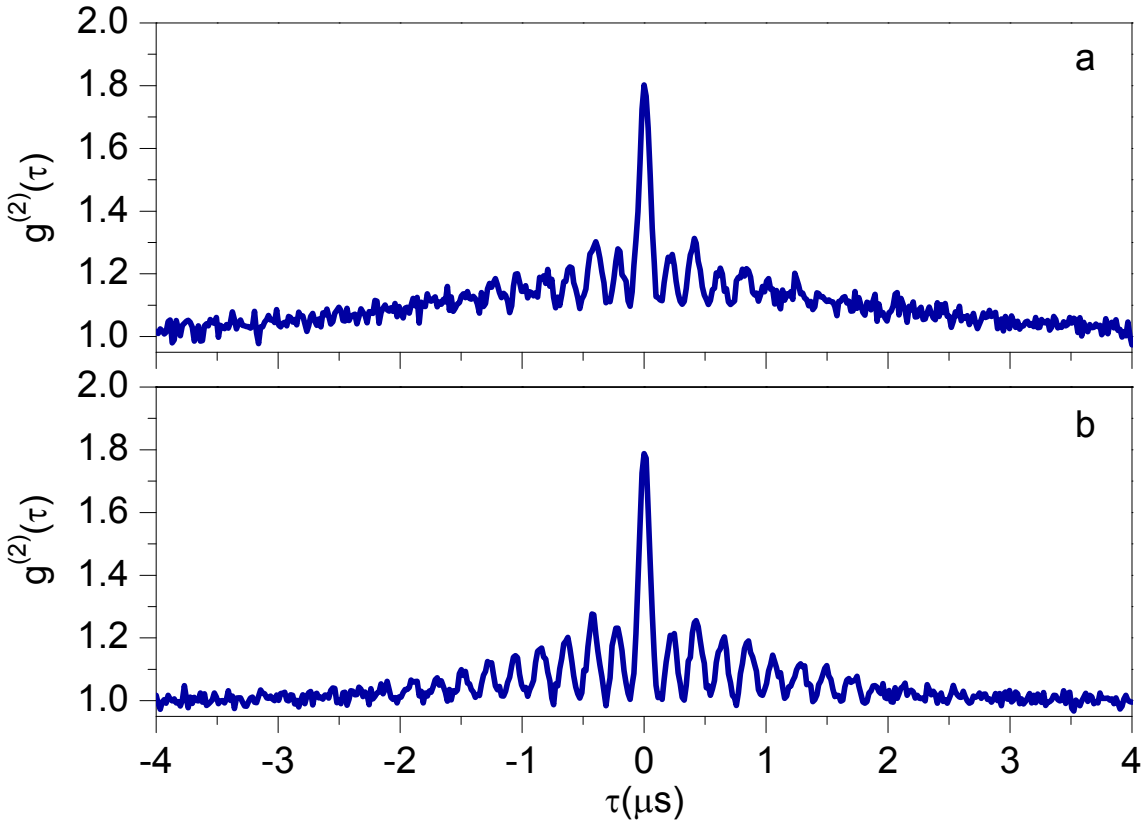

Figure 3.3: Intensity correlation function of the H mode for 4–6 photons in the V mode (when no atoms are present) and a 5 G magnetic field: a) $\bar{N} = 0.2$ and b) $\bar{N} = 2.0$.

3.3 Measurements

Figure 3.3a displays a measured correlation function at a magnetic field of 5 G, with a beat frequency of 4.9 MHz. The V mode is populated with 4–6 photons, on average, when no atoms are present, and the atomic flux corresponds to $\bar{N} \approx 0.2$ effective maximally coupled atoms; most of the time there are no atoms well-coupled to the mode [53]. The oscillation has low visibility and sits atop a raised Gaussian background whose correlation time is given by the transit time of an atom ($\approx 4\,\mu$s). The dominant beat for small $\bar{N}$ is that arising from the emission of two photons by the same atom (see Fig. 3.9c). Figure 3.3b displays the measured correlation function with $\bar{N}$ larger by a factor of 10 but otherwise similar conditions. The beat visibility is improved. The background is also removed, evidence that there is now an equal (at least) two-atom quantum beat (see Fig. 3.9d). The beat frequency is reduced to 4.7 MHz, an indirect effect of increased absorption by the additional atomic flux, which reduces the V-mode photon number—by a factor of two—and thus also the light shifts. A detailed study of light shifts is presented in Chapter 4.

Figure 3.4 shows a similar measured correlation function for a magnetic field of 4 G (A) and its calculated FFT power spectrum (B). The main peak near 3.5 MHz corresponds to the quantum beat resonance. A smaller peak at half this frequency is also visible, the result of homodyne interference with drive light mixed in by cavity birefringence (see discussion below). The small sidebands on the main peak correspond to a slight modulation of the beat envelope visible in (A). This is the result of the small (1–2°) deviation from normal incidence at which the atomic beam

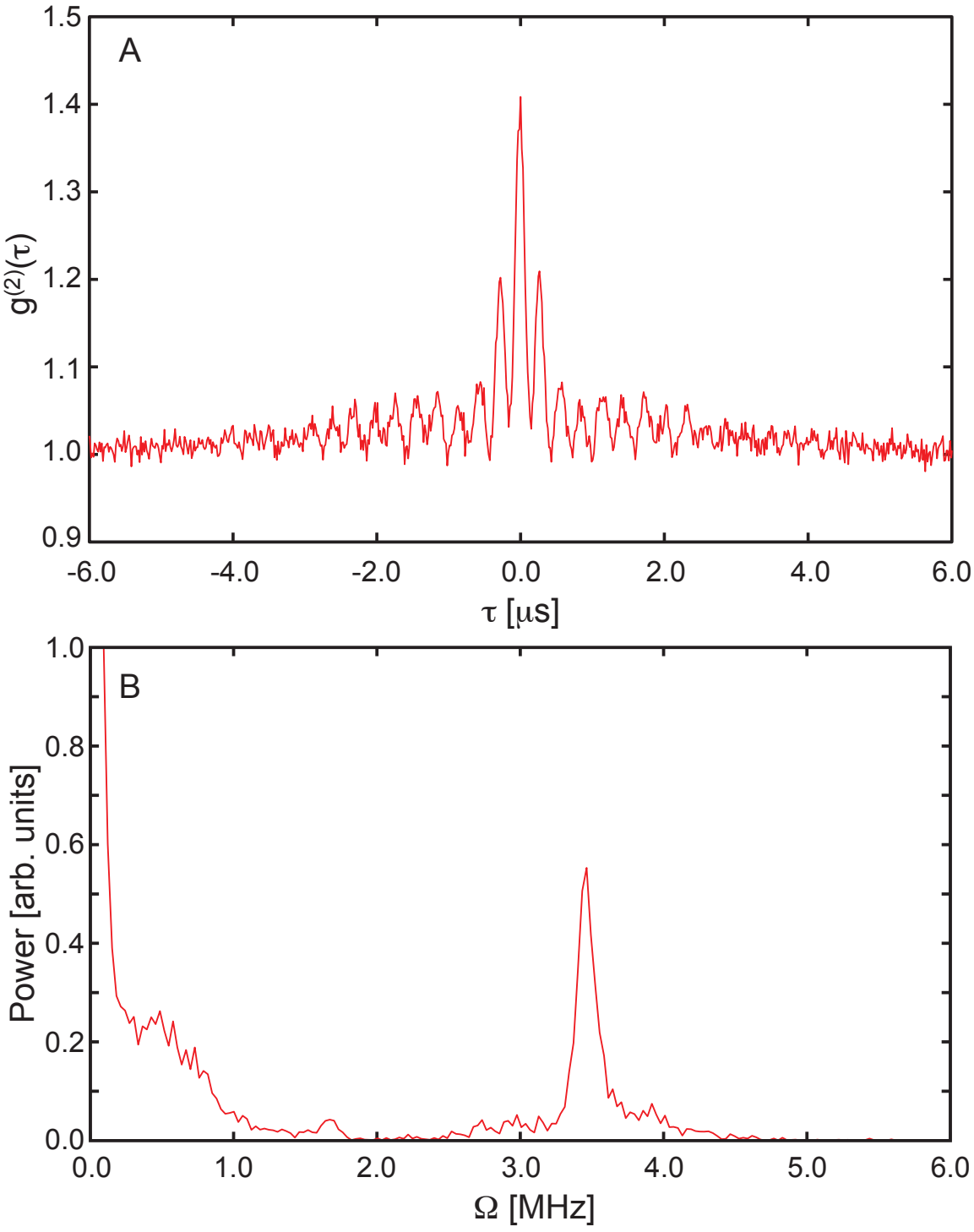

Figure 3.4: Intensity correlation function and spectrum. A) $g^{(2)}(\tau)$ measured at 4 G magnetic field. B) FFT power spectrum of data in (A). The peak at 3.5 MHz corresponds to approximately twice the Larmor frequency for the ground states in a 4 G field.

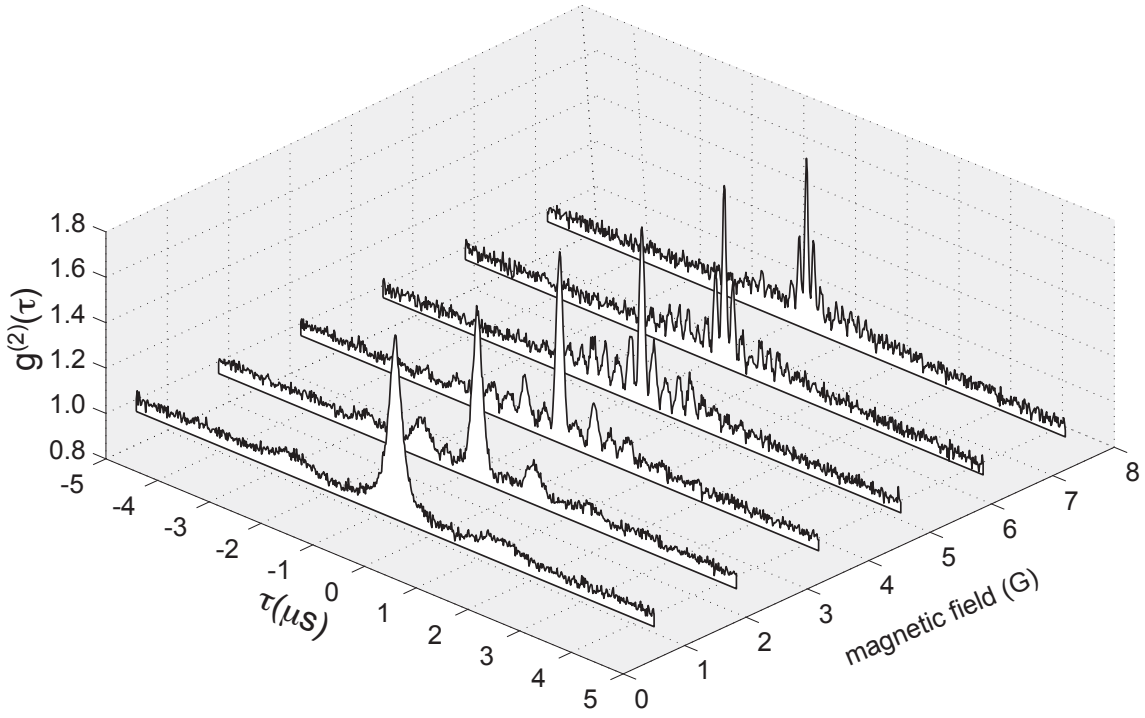

Figure 3.5: Evolution of $g^{(2)}(\tau)$ with increasing magnetic field.

traverses the cavity mode standing wave, resulting in a sinusoidally varying value of g and amplitude modulation in the spontaneous emission rate. (This is the same modulation envelope from Fig. 2.7.)

Figure 3.5 illustrates the change of the autocorrelation function with increasing magnetic field. The beat frequency increases while the envelope from the atomic transits stays constant. The beat visibility decreases for large magnetic field. Fig. 3.6 shows the effect of stronger driving on the beats. The amplitude of oscillation damps until at high drive only a thermal bunching peak remains. At even higher drives this peak also disappears, the result of the larger fraction of coherent light in the count rate, due to cavity birefringence and possibly the splitting of the sponta-

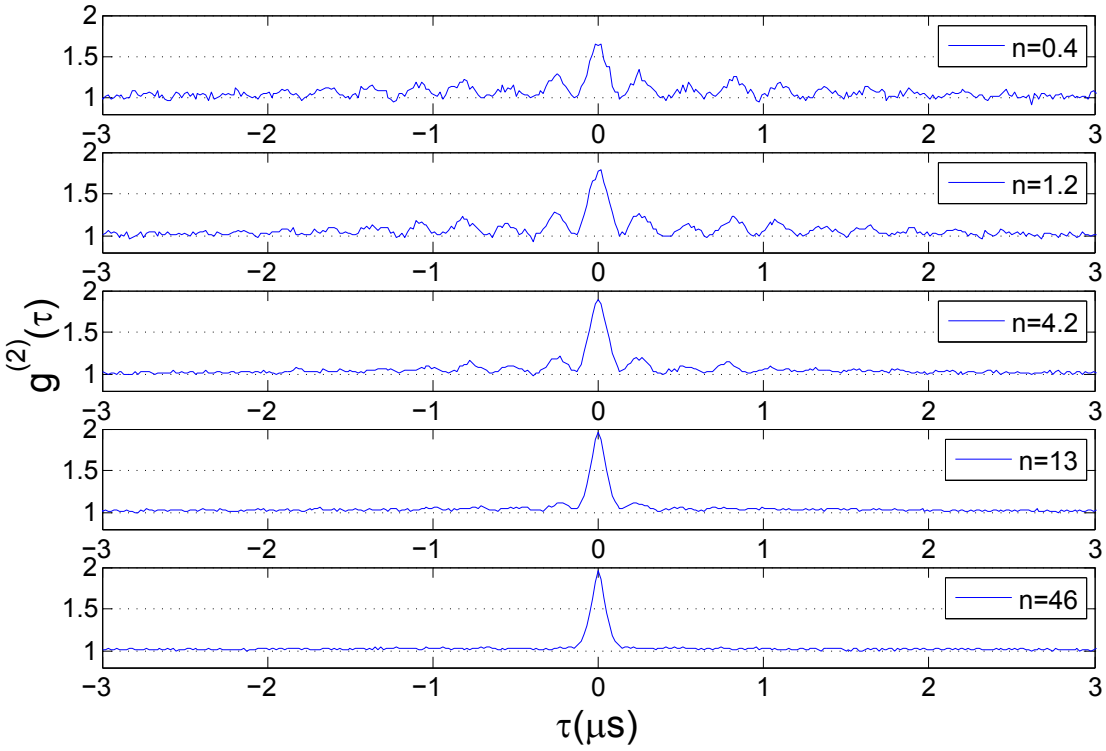

Figure 3.6: Evolution of $g^{(2)}(\tau)$ with increasing photon number in V.

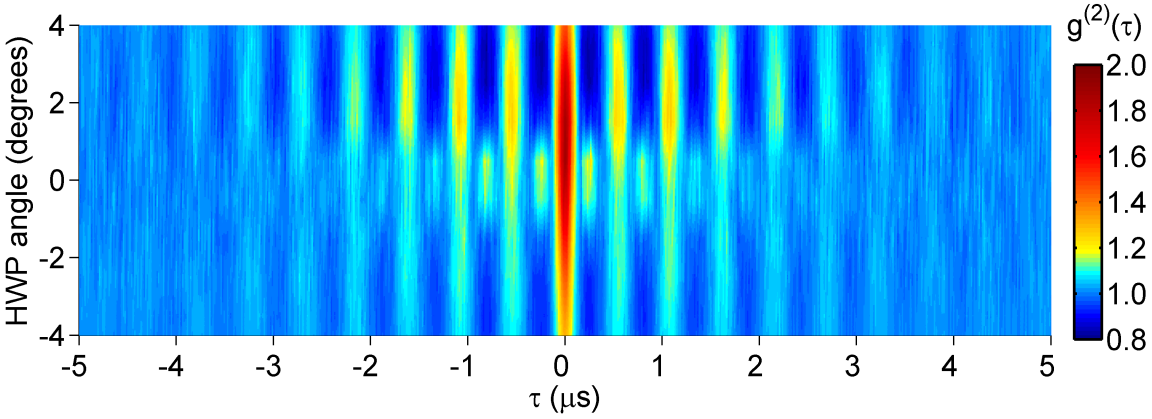

Figure 3.7: Evolution of the quantum beat as V-mode light is mixed with the H mode. Upper and lower extremes correspond to approximately six times more detector counts from the V mode than spontaneous emission. The parameters are 1.2 photons in the V mode, a magnetic field of 4 G, and $\bar{N} = 1$.

neous emission spectrum with strong driving. The mechanism for the disappearance of the beats in these two figures will be explained in Chapter 4.

Figures 3.7 and 3.8 illustrate the change in the observed beat when the polarization presented to the detector is not taken orthogonal to the polarization of the drive but is allowed to rotate by a few degrees. The rotation is controlled by changing the angle of the HWP placed between the cavity and the PBS (Fig. 3.1b). This mixes a small amount of drive light with the scattered light. With increasing fraction of drive light, the beat is eventually dominated by a homodyne term (Fig. 3.9e) arising from the correlation of a photon scattered into the H mode with a photon from the drive; thus, as in the two-atom case, interfering time orders yield a quantum beat. This beat oscillates at half the frequency and allows the correlation function to dip below one. Generally, some drive light is coupled into the H

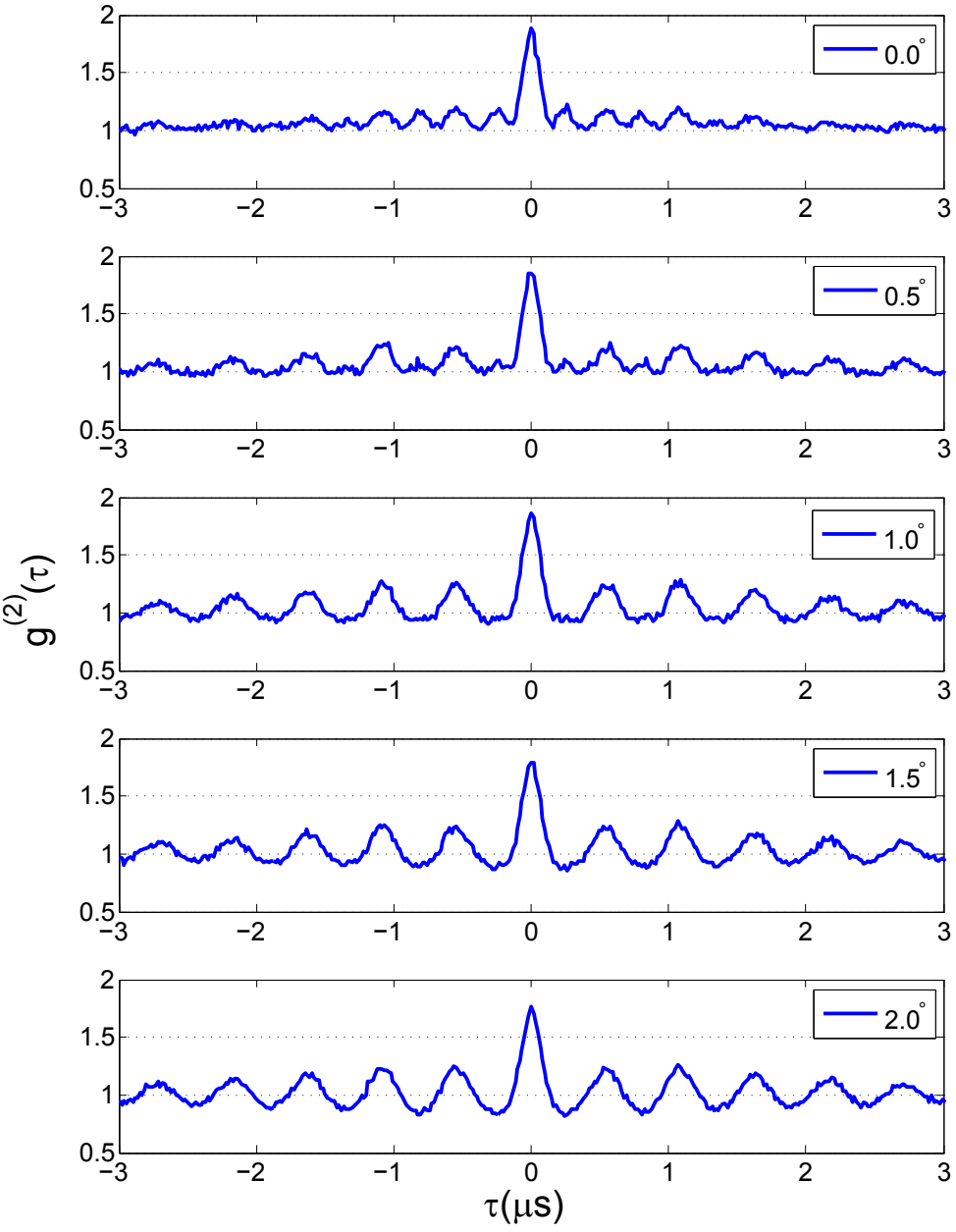

Figure 3.8: Evolution of $g^{(2)}(\tau)$ with homodyne mixing. Parameters as in Fig. 3.7, with angle of HWP labeled with respect to position of maximum extinction.

mode through a small birefringence of the cavity mirrors. In Fig. 3.7, the evident asymmetry with respect to angle is probably due to a small residual magnetic field component in the direction of the cavity axis.

Quantum trajectory simulations agree well with the measurements. Figure 3.9a displays a computed correlation function overlaying the data of Fig. 3.3b. A mean velocity of 22 m/s fits the decay of coherence well. Other parameters, such as the fidelity of the optical pumping, atomic beam tilt, and background from birefringence or elsewhere are more difficult to accurately determine (no background correction is made to the data). Note that with a background light amplitude β from birefringence, the post-detection state is $|\psi'\rangle + \beta|\psi\rangle$, and β carries noise from the atomic beam and spontaneous emission (absorption on the V mode). Plausible parameters are used for the plots of Fig. 3.9, with the quality of the fit primarily determined by the atomic beam density, which controls the relative size of the one- and two-atom quantum beats, and the strength of the drive, which controls the level of spontaneous emission. For the parameters of Fig. 3.9a, an atom passing near the cavity axis (within half a mode waist) typically undergoes ~ 10 spontaneous emissions to non-cavity modes during its transit, yet the coherence, merely passed between different m_i-multiplets, is preserved. In contrast, spontaneous emission decoheres an excited-state beat.

Figure 3.9b displays an example of a correlation function with mixed drive light (as in Fig. 3.7), together with its breakdown into three contributing quantum beats: one-atom interference (frame c), two-atom interference (frame d), and homodyne interference (frame e). The pieces lie in one-to-one correspondence with known

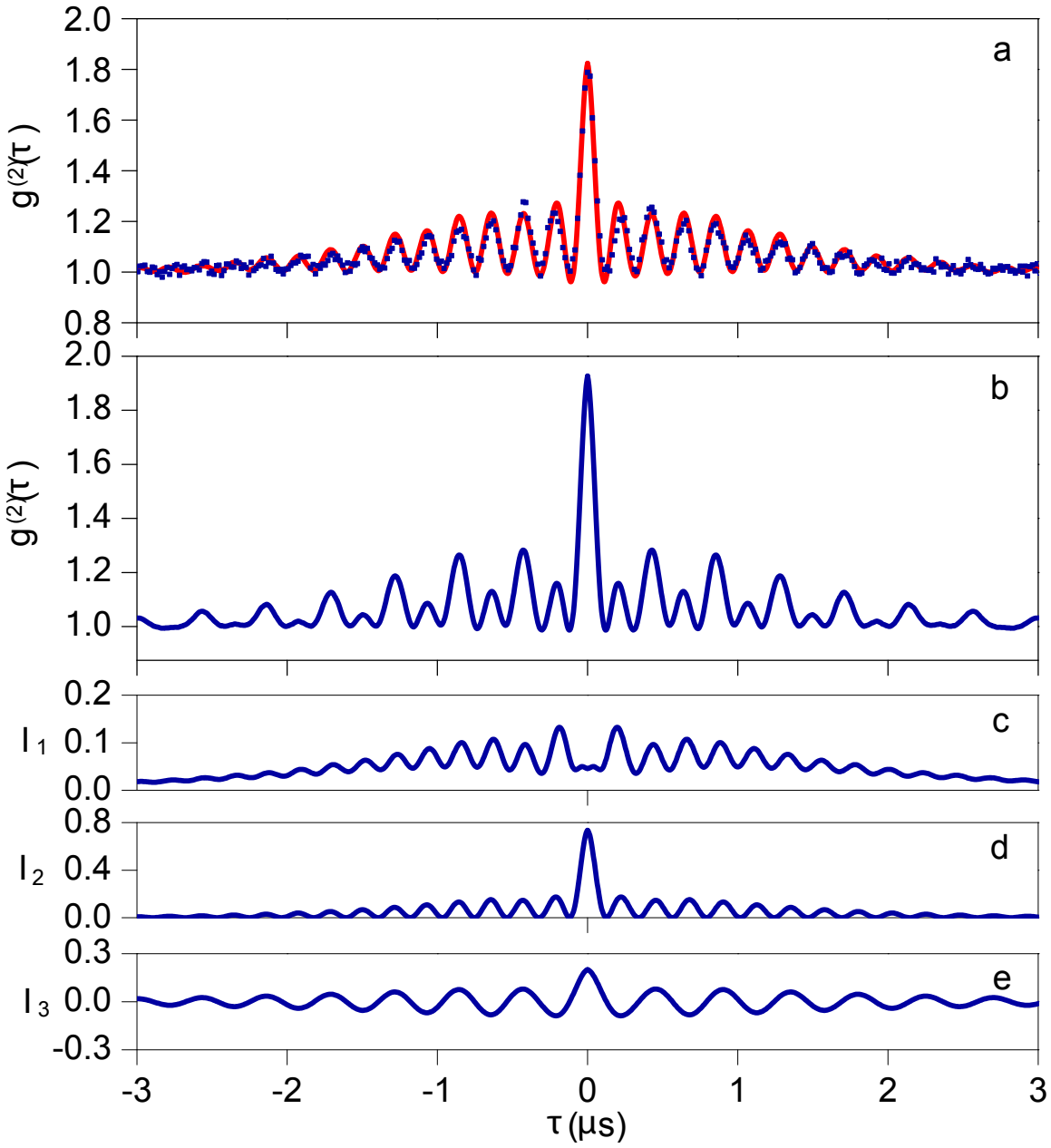

Figure 3.9: Calculated intensity correlation function with the birefringence background set at 1% a) and 10% b) of the H-mode photon number; c), d), e) the three interference terms contributing in b); curve a) is plotted against the data of Fig. 3.3 b). Parameters are $\bar{N} = 4$, 8 photons in the V mode with no atoms present, and an atomic beam tilt of 1.3 degrees.

terms in the intensity correlation function for a source comprised of many scatterers and a coherent background, e.g. Eq. (11) of [46], where the correlation function is the sum of a single-atom term, $g_A^{(2)}(\tau)$, two-atom term, $|g_A^{(1)}(\tau)|^2$, and a homodyne term, $\mathrm{Re}[\mathrm{g}_\mathrm{A}^{(1)}(\tau)]$.

Chapter 4

Backward Light Shifts and Quantum Jumps

4.1 Introduction

Spontaneous emission is a fundamental damping mechanism for coherence stored in optically driven atoms [72]. At random intervals, the atomic dipole between ground and excited energy levels disappears in a sudden projection onto a single state, an event referred to as a "quantum jump" [12]. Under certain conditions quantum jumps are directly observable in the measurement record, as when an atom jumps intermittently between "bright" and "dark" states [73, 74]; experimental measurements of switching in atomic [75, 76, 77] and photonic [8] systems provide clear visualization of the discrete nature of the dynamics. Although quantum jumps often bring decoherence and spectral broadening–they give breadth to the natural linewidth of resonance fluorescence–certain coherences may also be preserved or even created in these processes under appropriate conditions [58, 65].

In contrast to the dynamical energy changes associated with quantum jumps in a driven atom, light coupled to an atomic transition can also induce a structural change in the energy levels through the AC Stark shift [78]. The energy eigenvalues move in a direction determined by the sign of the light detuning from resonance, but populations and coherences among the levels are preserved. For example, the ground states of Fig. 4.1 exhibit equal but opposite AC Stark shifts when the laser

is tuned halfway between the two π transitions; the energy of $|g_+\rangle$ decreases and the energy of $|g_-\rangle$ increases, reducing the ground-state energy separation (a negative differential light shift.) When preservation of coherence is paramount, quantum state manipulation with lasers is typically performed far from resonance, where the AC Stark shift is large but the spontaneous emission rate is small [79, 80]. Perhaps for this reason, the evolution of coherence in the opposite regime, where AC Stark shifts coexist with a large spontaneous emission rate, has not been exhaustively investigated.

In this chapter we present measurements on a system near resonance where high rates of spontaneous emission and quantum jumps not only preserve but dynamically *modify* a coherence, effectively changing the sign of the ground-state differential light shift of the configuration illustrated in Fig. 4.1. Our analysis generalizes a decoherence mechanism in Rayleigh scattering recently reported in the literature [81]. We show that it encompasses a coherent as well as incoherent aspect, depending on the size of the detunings.

4.2 Experimental system

We measure differential light shifts in a beam of cold ^{85}Rb atoms passing through an optical cavity, using a ground-state interference technique [58]. A vertically polarized cavity mode, V, is weakly driven with coherent light at 780 nm and oriented with polarization vector parallel to a weak magnetic field (see Fig. 4.2).

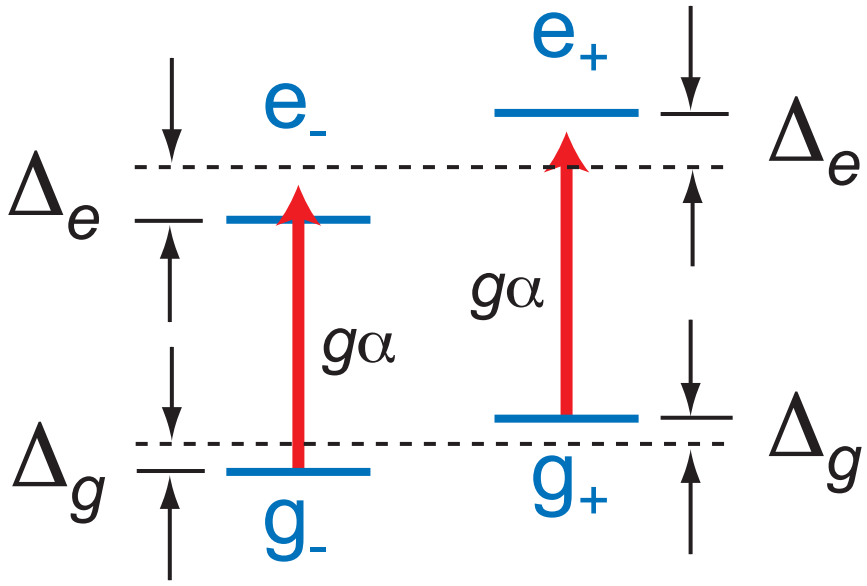

Figure 4.1: Four-level atom with unequal Zeeman shifts in the ground (Δ_g) and excited (Δ_e) states. A coherent field α is resonant with the unshifted transition between ground and excited states (dashed lines) and drives the two π transitions with equal coupling constants g. σ transitions (not shown) allow the spontaneous creation of an initial coherence between the ground states, starting from an unshifted and driven $m = 0$ to $m' = 0$ transition.

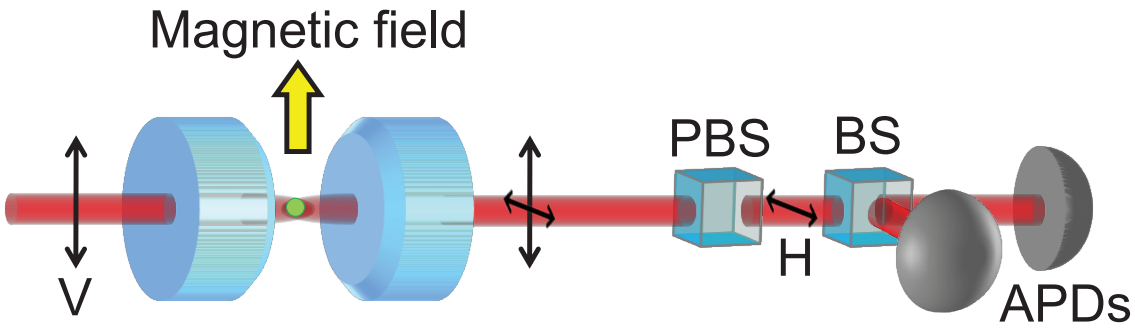

Figure 4.2: Schematic of the apparatus for measuring $g^{(2)}(\tau)$, with a single atom represented in green and the magnetic field inside the cavity aligned to the exciting polarization; PBS: polarizing beam-splitter, BS: beam-splitter, APD: avalanche photodiode.

Photons in V excite π transitions in the atoms between the $F = 3$ and $F' = 4$ manifolds, and also cause light shifts when a detuning exists between a transition frequency and the laser frequency. A degenerate but horizontally polarized mode, H, collects photons emitted spontaneously on σ transitions between the same two manifolds; these photons have a bandwidth similar to that of the cavity, and can be distinguished from those of the drive by polarization. Detection of a photon from H spontaneously creates a coherent superposition among the magnetic ground states, and conditional detection of a second photon from H reads out the coherence. This setup enables a direct measurement of the Zeeman energy splitting of the ground states as the frequency of a long-lived quantum beat in the intensity autocorrelation function $g^{(2)}(\tau)$. The measurement is sensitive to a differential light shift of the ground states, which appears as an intensity-dependent change in the beat frequency; and also to decoherence of the spontaneously-created superpositions, which appears as a broadening of the resonance in the power spectrum of $g^{(2)}(\tau)$.

Examples of the beat signals taken from a full quantum Monte Carlo simulation of our system appear in Fig.4.3, and from recorded data in Fig.4.4. Both show the frequency of oscillation increasing as a function of average photon number in V, evidently the result of a light shift. However, this behavior is contrary to that expected from the AC Stark shift; our system roughly corresponds to the situation depicted in Fig. 4.1, since most atoms are in a superposition of the $m = \pm 1$ ground states while the laser is resonant with the unshifted $m = 0$ to $m' = 0$ transition. Stronger driving rapidly damps the coherence, bringing faster decay times to the oscillations.

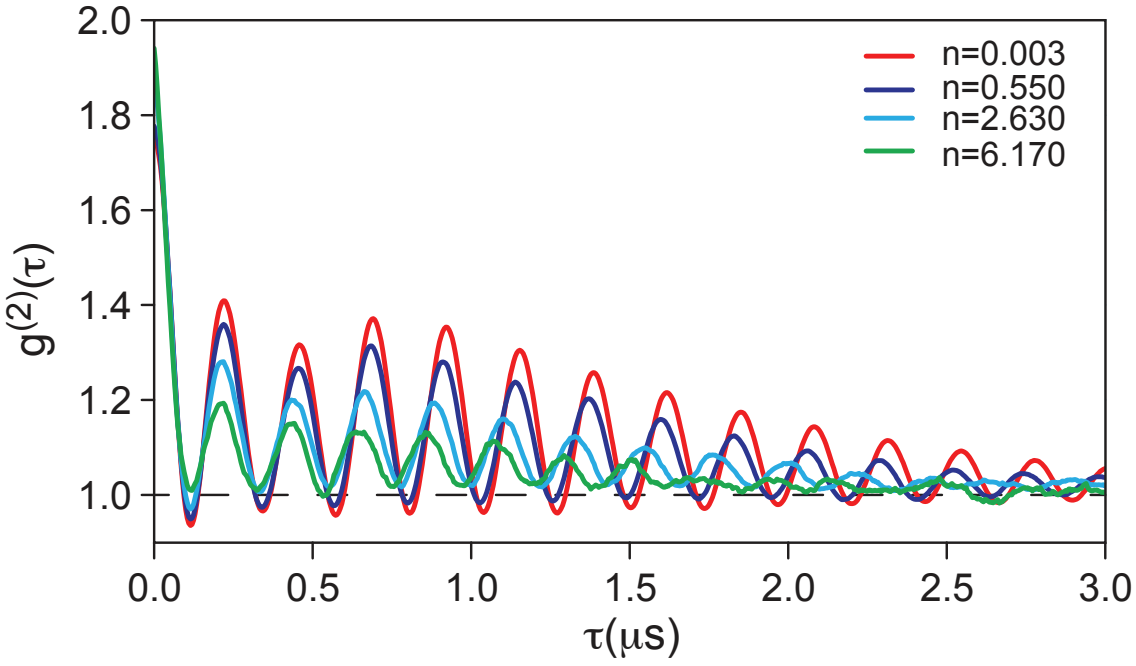

Figure 4.3: Quantum Monte Carlo simulation of intensity autocorrelation signal from H for four different photon numbers n in the driven mode V. (**B**) Composite experimental autocorrelation data as in (A) with amplitude color scaled to show detail.

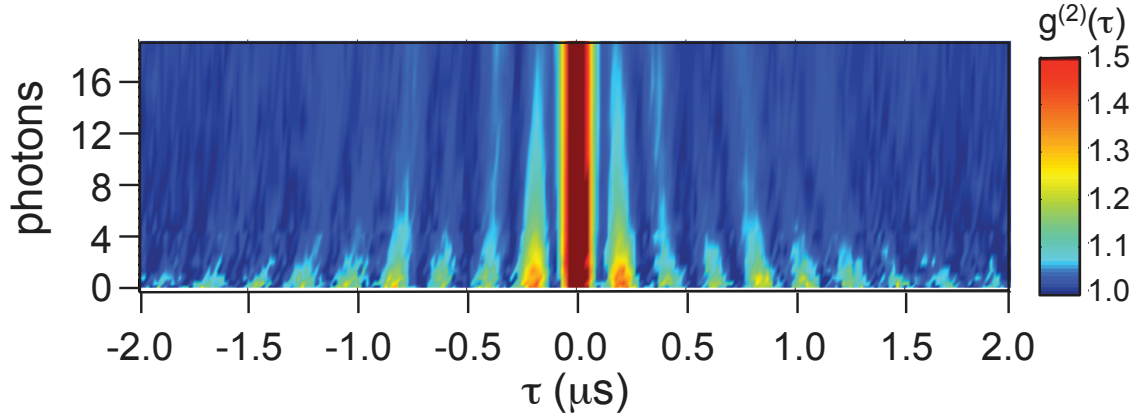

Figure 4.4: Composite experimental autocorrelation data as in Fig. 4.3 with amplitude color scaled to show detail.

4.3 Theoretical model

We explain the origin of the light shifts and damping with the four-level atom shown in Fig. 4.1, using the quantum trajectory formalism [12]. Our analysis applies generally to any quantum system of this type and does not explicitly require a cavity, which essentially provides a spatial mode for the optical excitation and detection.

The system is prepared at time $t = 0$ in the ground-state superposition $|\psi\rangle = \frac{1}{\sqrt{2}}(|g_-\rangle + |g_+\rangle)$. (This occurs spontaneously in our apparatus after detection of a single photon from H.) The weak coherent drive couples the ground and excited states, with coefficients satisfying the equations:

$$\begin{aligned} \dot{c}_{e\pm} &= -\frac{\gamma}{2}c_{e\pm} \mp i\Delta_e c_{e\pm} + g\alpha c_{g\pm}, \\ \dot{c}_{g\pm} &= \mp i\Delta_g c_{g\pm} - g\alpha^* c_{e\pm}, \end{aligned} \tag{4.1}$$

where $g\alpha$ is the Rabi frequency, and Δ_g and Δ_e are ground and excited-state Zeeman shifts. The ground-state superposition evolves in time as:

$$|\psi_g(t)\rangle = \frac{1}{\sqrt{2}}(e^{i(\Delta_g+\Delta_{AC})t}|g_-\rangle + e^{-i(\Delta_g+\Delta_{AC})t}|g_+\rangle), \tag{4.2}$$

where

$$\Delta_{AC} = -\frac{g^2|\alpha|^2\Delta}{(\gamma/2)^2 + \Delta^2} \tag{4.3}$$

is the ground-state AC Stark shift obtained from diagonalizing Eqs. 4.1 to lowest order in $g^2|\alpha|^2$, and $\Delta = \Delta_e - \Delta_g$ is the magnitude of the laser detuning from each transition as depicted in Fig. 4.1. The differential ground-state AC Stark shift is $2\Delta_{AC}$, and it *reduces* the ground-state Zeeman splitting.

Under weak driving and with no quantum jumps, the amplitudes in Eq. 4.2 drive a steady-state superposition in the excited state:

$$|\psi_e(t)\rangle = \left(\frac{g\alpha}{\sqrt{2}}\right)\left(\frac{e^{i(\Delta_g+\Delta_{AC})t}}{\gamma/2 - i\Delta}|e_-\rangle + \frac{e^{-i(\Delta_g+\Delta_{AC})t}}{\gamma/2 + i\Delta}|e_+\rangle\right). \tag{4.4}$$

The amplitudes of Eq. 4.4 oscillate at the ground-state splitting; the excited-state splitting enters only through the factors $\gamma/2 \pm i\Delta$, which imply a phase shift. Interference of the amplitudes in Eq. 4.4 produces the quantum beats which we measure.

We show now that spontaneous emission in the form of quantum jumps adds both a coherent and incoherent contribution to the time evolution, changing the measured differential light shift from $2\Delta_{AC}$ to $-2\Delta_{AC}$, while at the same time decohering the ground-state superposition. (Here for simplicity we consider only π jumps occurring in between the measured σ emissions; additional σ jumps serve only to pump the coherence elsewhere in the manifold, changing Rabi frequencies and adding additional detunings.) At jump rate $\Gamma = \gamma g^2|\alpha|^2/((\gamma/2)^2 + \Delta^2)$, the driven dipole between ground and excited states turns off and the amplitudes of Eq. 4.4 are transferred to the ground states; in place of Eq. 4.2:

$$|\psi_g(t)\rangle = \frac{1}{\sqrt{2}}\left[\frac{\gamma/2 + i\Delta}{\sqrt{(\gamma/2)^2 + \Delta^2}}e^{i(\Delta_g+\Delta_{AC})t}|g_-\rangle + \frac{\gamma/2 - i\Delta}{\sqrt{(\gamma/2)^2 + \Delta^2}}e^{-i(\Delta_g+\Delta_{AC})t}|g_+\rangle\right], \tag{4.5}$$

where the ground-state superposition has acquired a phase advance. The process repeats for additional quantum jumps, so the phase advance accumulates over time. For a jump rate Γ, we average the $|g_+\rangle\langle g_-|$-coherence against a Poisson distribution of mean Γt, to obtain the expectation value of the ground-state coherence:

$$\rho_{g+,g-} = e^{-2i(\Delta_g+\Delta_{AC})t}\frac{1}{2}\sum_{n=0}^{\infty}\left(\frac{(\gamma/2 - i\Delta)^2}{(\gamma/2)^2 + \Delta^2}\right)^n \frac{(\Gamma t)^n}{n!}e^{-\Gamma t}$$

$$= \quad e^{-2i(\Delta_g+\Delta_{AC})t}\frac{1}{2}e^{-(\Gamma_{decoh}+i2\Delta_{jump})t}. \tag{4.6}$$

The imaginary part of the exponent contains a new term, $-2\Delta_{jump}t$, where

$$\Delta_{jump} = \Gamma\frac{\Delta\gamma/2}{(\gamma/2)^2+\Delta^2} = 2g^2|\alpha|^2\Delta\left(\frac{\gamma/2}{(\gamma/2)^2+\Delta^2}\right)^2. \tag{4.7}$$

This term represents an additional frequency shift arising from the mean rate of phase accumulation from quantum jumps. It is opposite in sign to the AC Stark shift brought by the same driving laser (Eq. 4.3), and bigger than the AC Stark shift by a factor of two when the detuning is small (i.e. when $\Delta \ll \gamma/2$). The net differential ground-state light shift in this case becomes

$$2\Delta_{light} = 2(\Delta_{AC}+\Delta_{jump}) \approx -2\Delta_{AC}, \tag{4.8}$$

with the sign of the differential AC Stark shift effectively reversed. The effect requires at least the structure of a four-level atom, since jumps bring only an unobservable overall phase shift in a two-level atom.

The exponent in Eq. 4.6 also contains a damping term, $-\Gamma_{decoh}t$, which decoheres the quantum beats at a rate

$$\Gamma_{decoh} = \Gamma\frac{2\Delta^2}{(\gamma/2)^2+\Delta^2} = 2g^2|\alpha|^2\gamma\left(\frac{\Delta}{(\gamma/2)^2+\Delta^2}\right)^2. \tag{4.9}$$

The origin of the decoherence is phase diffusion of the ground-state superposition, which accompanies the net phase drift that constitutes the frequency shift. Both aspects are expected from the stochastic nature of the jump process. Noting that $\Gamma_{decoh}/(2\Delta_{jump}) = 2\Delta/\gamma$, we may speak of a well-resolved frequency shift when $\Delta \ll \gamma/2$. When this condition is not met, a single jump can result in a phase

change of π, smearing out the fringes over multiple measurements. In general, we require the product of the jump number fluctuation with the phase shift per jump to be much less than π in order to maintain coherence in the averaging process. Increasing the magnetic field (Δ) or the drive strength (Γ) causes this product to increase; this is the origin of the beat decoherence presented in Chapter 3.

The above analysis is valid for a four-level atom with constant coupling strength to a weak coherent drive. Our experimental system brings many additional complications. These include optical pumping within the full level structure of ^{85}Rb, a finite interaction time with the laser and fluctuations in coupling strength due to the atomic beam traversing the cavity mode, (weak) multi-atom and cavity effects, and saturation behavior with strong driving. For these reasons we implement the theory as a full quantum Monte Carlo calculation in order to make quantitative comparison with our measurements [58].

4.4 Data analysis

We analyze the data by calculating the Fast Fourier Transform (FFT) amplitude spectrum of each measured $g^{(2)}(\tau)$ and extracting the center frequency and FWHM of each ground-state beat resonance peak. Figure 4.5 shows the weak drive region for four different magnetic field values, with linear fits to the data as dashed lines; the slope increase is approximately linear with magnetic field (detuning). We extract the natural (non-light-shifted) Larmor frequency for each magnetic field value by extrapolating this portion of data to n=0. This point corresponds to the

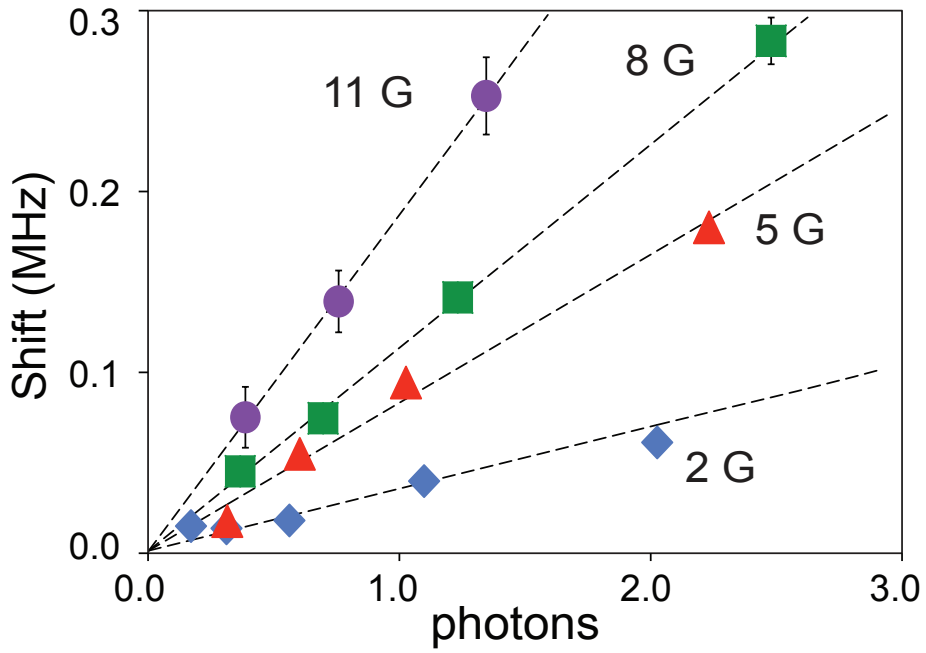

Figure 4.5: Center frequency of beat resonance at low photon number for four magnetic field values. The dashed lines are linear fits to the data used to extrapolate the unshifted beat frequency. In all the following figures, error bars show ± one standard deviation confidence intervals of Voigt profile fits to the resonance peaks. Experimentally determined photon numbers have an uncertainty of 20%.

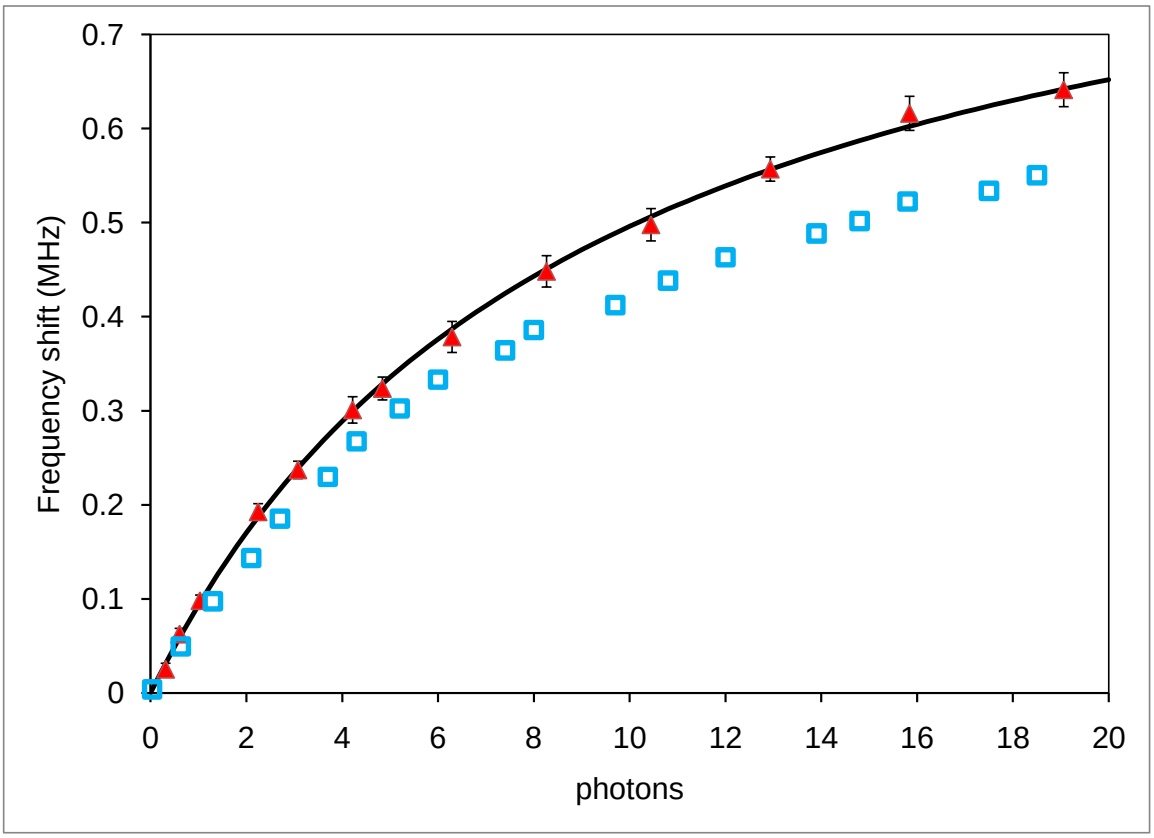

Figure 4.6: Center frequency of beat resonance versus photon number in V from FFTs of measured data (red filled triangles) and simulations (blue open squares). The solid line is a fit to a simple saturation functional form.

unshifted beat frequency $2\Delta_g = 2\mu_B B_{mag}/3$, where μ_B=1.4 MHz/G is the Bohr magneton and B_{mag} is the magnitude of the magnetic field. From this frequency we extract the value of B_{mag} and the detuning, $\Delta = \Delta_g/2$.

Figure 4.6 tracks the frequency shift (red filled triangles) for the data of Fig. 4.4, where a shift of 0 MHz corresponds to the natural Larmor frequency of 4.7 MHz at 5 G magnetic field. The results taken from the quantum Monte Carlo calculations are plotted as blue empty squares. The difference between the two is primarily due

to the experimental uncertainty in intracavity photon number.

We find that despite the complications, the data points in the high intensity region are described well by considering saturation of the jump rate as in a two-level atom, i.e. $\Gamma \to (\gamma/2)(n/n_{\rm sat})/(1+n/n_{\rm sat})$, where $n_{\rm sat} \equiv \gamma^2/(8g^2)$ is the saturation photon number for a two-level atom in a cavity. In the absence of optical pumping effects, the effective saturation photon number for an atom in the $m = \pm 1$ ground states of our system should be $n_{\rm sat} = \gamma^2/(3g_{\rm max}^2) = 5.7$ photons, where $g_{\rm max}$ is the peak value of g at the center of an antinode of the cavity Gaussian standing wave mode function, and a factor of 3/8 has been included to account for the averaging of g^2 over the mode structure.

To match the frequency shift data in Fig. 4.6, we use the simple saturation form for Γ together with Eq. 4.8 at lowest order in Δ:

$$2\Delta_{light} = \frac{A_{\rm shift}\Delta(n/n'_{\rm sat})}{1+n/n'_{\rm sat}}.$$

We expect the effective saturation photon number $n'_{\rm sat}$ to be larger than $n_{\rm sat} = 5.7$ as optical pumping puts the population in states with weaker coupling to the mode and larger detunings. The scale factor of $A_{\rm shift}$ is to include any other optical pumping and detuning effects. The two-parameter least-squares fit shown by the solid line in Fig. 4.6 gives $A_{\rm shift} = 0.81 \pm 0.01$, $n'_{\rm sat} = 9.2 \pm 0.2$, with a reduced $\chi^2 = 0.32$. The statistical error bars in all the figures are the 68.3% confidence intervals for the given parameter (center frequency or linewidth) from a least-squares fit of each FFT resonance peak to a Gaussian profile.

Figure 4.7 shows the onset of decoherence with stronger driving, as extracted

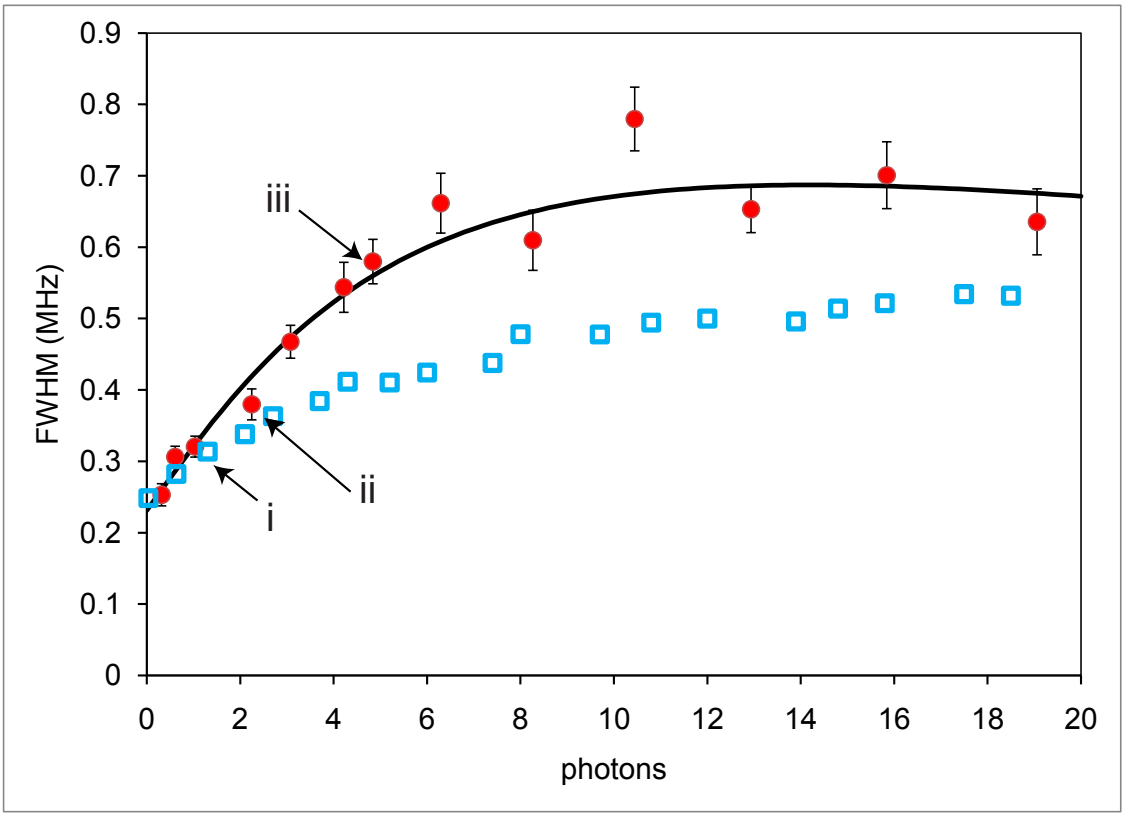

Figure 4.7: FWHM of beat resonance versus photon number in V for measured data (red filled circles) and simulations (blue open squares). The solid line is a fit to the data for a simple saturation functional form.

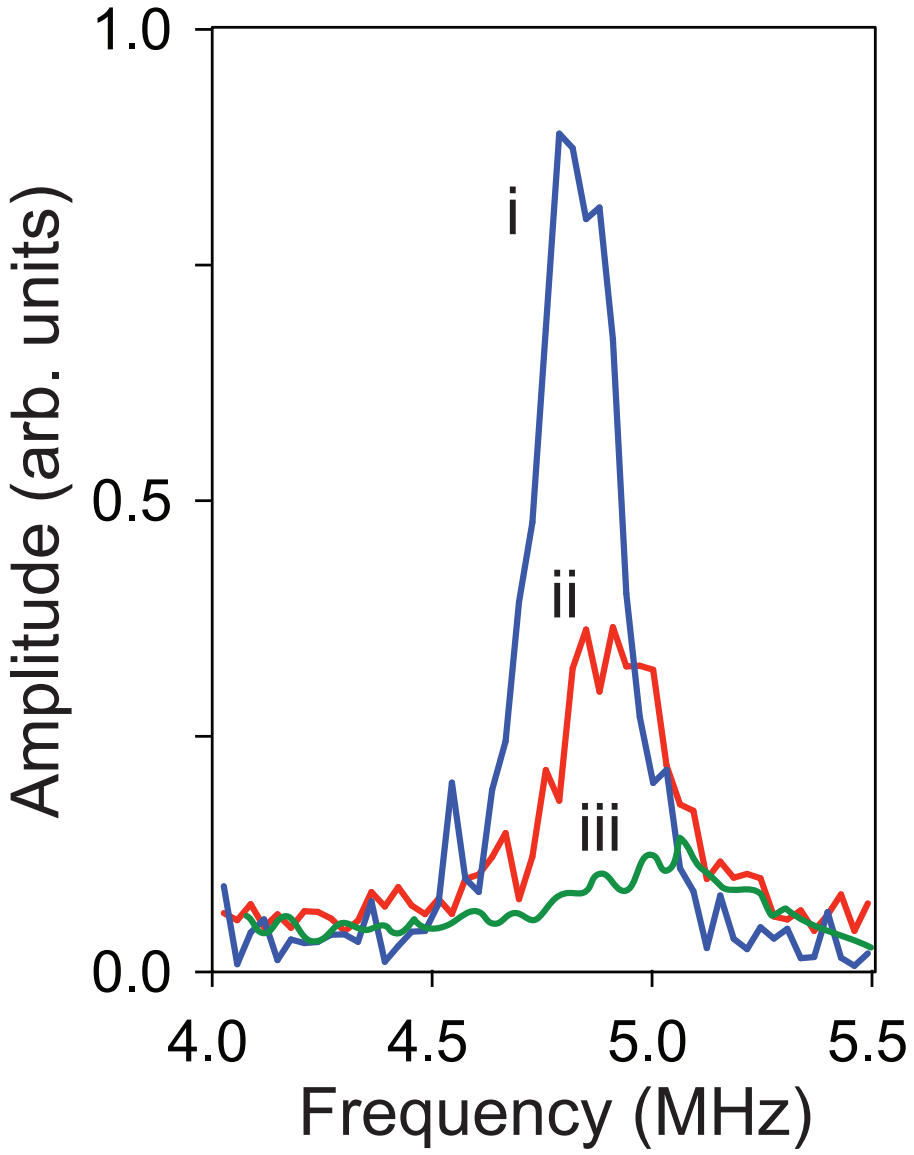

Figure 4.8: Three sample peaks from FFT amplitude spectra showing shifts and broadening with increased drive; the labels refer to the three points in Fig. 4.7 (i, ii, and iii).

from the widths of the resonance peaks from measured data (red filled circles) and from the quantum Monte Carlo simulation (blue empty squares). The zero-photon linewidth (0.23 MHz) arises from the finite transit time of the atoms traversing the Gaussian cavity mode. To match the data, we apply a similar saturation form as above to Eq. 4.9, at lowest order in Δ:

$$\Gamma_{decoh} = \frac{A_{\rm width}\gamma(n/n'_{\rm sat})(2\Delta/\gamma)^2}{1 + n/n'_{\rm sat}}.$$

We convolve this Lorentzian width with the Gaussian FWHM arising from the atom transits, $2\Gamma_{gauss} = 2\pi \times 0.23$ MHz, in a Voigt profile, using the numerical approximation:

$$2\Gamma_{voigt} \approx 0.5346(2\Gamma_{decoh}) + \sqrt{0.2166(2\Gamma_{decoh})^2 + (2\Gamma_{gauss})^2}.$$

A two-parameter least-squares fit to the composite width (solid line) gives $A_{\rm width} = 1.31\pm0.03$, $n'_{\rm sat} = 14.2\pm0.5$, with a reduced $\chi^2 = 1.6$. Fig. 4.8 shows the broadening and shift of three sample resonance peaks from the experimental data.

The results of the four-level model can be extended to include a detuning of the drive laser from the unshifted (zero magnetic field) transition frequency (dashed lines in Fig. 4.1), denoted below as δ. The formulas for the differential ground-state light shift and decoherence rate become:

$$2\Delta_{light} = 2(\Delta_{AC} + \Delta_{jump}) = 2g^2|\alpha|^2\Delta\frac{(\gamma/2)^2 - \Delta^2 + \delta^2}{[(\gamma/2)^2 + (\delta+\Delta)^2][(\gamma/2)^2 + (\delta-\Delta)^2]} \tag{4.10}$$

and

$$\Gamma_{decoh} = 2g^2|\alpha|^2\gamma\frac{\Delta^2}{[(\gamma/2)^2 + (\delta+\Delta)^2][(\gamma/2)^2 + (\delta-\Delta)^2]}. \tag{4.11}$$

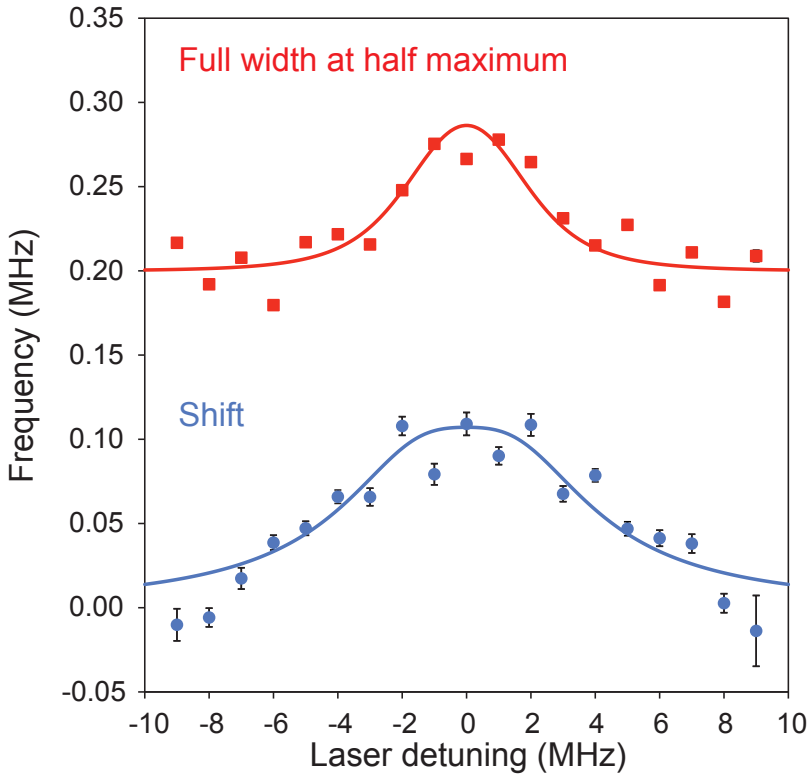

Figure 4.9: Sensitivity of light shift and linewidth to drive detuning δ from the central (zero magnetic field) transition frequency, with 5 G magnetic field and n =2 photons in V. Blue circles show shift in the center frequency from the zero-intensity value of 4.6 MHz, and red squares show the resonance FWHM. The solid lines are two-parameter fits to Eqs. 4.10 and 4.11. Error bars show ± one standard deviation confidence intervals of Gaussian profile fits to the resonance peaks, and for the case of the linewidths are smaller than the squares used to plot the points.

Figure 4.9 presents the predicted and measured detuning dependence at a magnetic field of 5 G. The photon number inside the cavity is kept constant at $n = 2$ photons, compensating for the off-resonant response of the cavity and atoms. The frequency shift (blue circles) decreases in both directions away from resonance. We fit the data to Eq. 4.10 (blue line) with an amplitude scaling factor A_{shift}, while keeping the same value obtained before for n'_{sat}, which effectively scales g^2 for the multi-level atomic structure. We find $A_{\text{shift}} = 0.71 \pm 0.01$ with a reduced $\chi^2 = 7.6$, due to a poor fit at large detuning and some possible fine structure at small.

The resonance peak width (red squares) presents a similar structure, reducing to the limiting value of 0.20 MHz (atom transit width) at a detuning of approximately 10 MHz, where the differential phase shift from each quantum jump is approximately zero. The red line is a fit to Eq. 4.11 convolved with transit broadening, with amplitude scaling as a free parameter. We find $A_{\text{width}} = 0.64 \pm 0.01$ for Eq. 4.11, with an order-of-magnitude discrepancy between the statistical error bars from the resonance peak fits and the fluctuations about the theoretical form.

4.5 Comparisons

Our results generalize the work of Uys *et al.* [81], who analyzed the effect of Rayleigh scattering on the decoherence of trapped ion qubits. Their result is recovered from Eq. 4.11 in the limit $\Delta \gg \gamma/2$, i.e. under conditions where jumps rarely occur but each carries a π phase shift, fully destroying the ground-state coherence. More generally the character of the decoherence differs depending on

the relative sizes of Δ, δ, and $\gamma/2$.

We have presented in the above an analysis of ground-state superpositions driven weakly by coherent light. A related situation was investigated by Cohen-Tannoudji [82, 83], who studied atoms excited by broadband thermal light. In this case, the ground-state superposition (induced by an external RF field) jumps at random times completely to an excited-state superposition, with no coherent dipole between ground and excited states, and the Larmor frequency changes from $2\Delta_g$ to $2\Delta_e$. Remaining in the excited state for an average time of $1/\gamma$, the relative phase advance per jump is thus $2(\Delta_e - \Delta_g)/\gamma = 2\Delta/\gamma$. This should be compared to the coherent driving case, where the relative phase advance per jump is $4\Delta/\gamma$ (from Eq. 4.5 with $\Delta \ll \gamma/2$.) The extra factor of two arises because the damping rate for the dipole is $\gamma/2$, in contrast to the damping rate for the population, which is γ; however, there is no AC Stark shift for broadband light near resonance, so the net light shift in the two cases is exactly the same when $\delta = 0$. This is a remarkable result, considering that the situations differ completely in detuning dependence and require entirely separate physical descriptions. We also note that the effect with coherent drive is five orders of magnitude larger than that observed previously with thermal light [82, 84, 85] and thus may need to be considered in some applications.

Chapter 5

Conclusions and Future Directions

The experimental results reported in this thesis all rely on conditional measurements of light from one mode of an optical cavity that probe the atom-cavity interactions occurring in the other mode. Although the basic concept of the apparatus is simple, the complexity of the components–in particular the presence of an atomic beam, multi-level atoms, and a mode-matched source of background light–has allowed observation of several surprising effects that may not appear in simpler systems, e.g. in ones optimized for quantum information applications and precise state control.

We demonstrated in Chapter 2 that a two-mode cavity QED system can function as a high-fidelity detector of single atoms. Our method can operate with a wide range of photon fluxes and works for atoms traveling as fast as 20 m/s across the mode. Because the cavity is frequency-selective and has a short lifetime (approximately equal to the atomic excited-state lifetime), the method guarantees that the atom is in the $F = 3$ hyperfine ground state immediately after the detection of the second photon. The scheme is sensitive enough to work without strong coupling of the cavity and atoms, meaning that the detection volume can be kept large. We also demonstrated how autocorrelation measurements of the emitted light show the underlying dynamics of the atom as it traverses the Gaussian mode of the cavity

and encounters the standing wave.

In Chapter 3 we presented observations of ground-state quantum beats in the spontaneous emission from a continuously driven atomic ensemble. Contrasting deterministic manipulations [62, 63], we demonstrated the spontaneous creation and readout of ground-state coherence, where in the spirit of Forrester *et al.* [61], we retrieve a hidden beat from the fluctuations. Our theoretical treatment via a quantum Monte Carlo calculation, which is in good agreement with the measurements, decomposes the signal into a one-atom beat, a two-atom beat (interference of emission time order), and a homodyne beat due to interference with a drive photon mixed through birefringenece.

In Chapter 4 we reported evidence of repeated quantum jumps modifying the spontaneously-generated coherence without destroying it, as a net drift guiding a stochastic phase diffusion. We presented a microscopic quantum trajectory model that gives an intuitive explanation of the light shifts, and which also explains the state decoherence at large detuning reported in Ref. [81]. Moreover, our results suggest the tantalizing possibility of using dissipation as an additional tool for coherent control.

Future upgrades to the experimental apparatus are planned. These include adding additional viewports to the cavity chamber to allow for better control of atomic state initialization as well as to give optical access to the cavity from the side; building a new cavity with slightly stronger coupling strength and much smaller absorptive photon losses; and implementing optical focusing of the atomic beam to increase the density of atoms in the cavity. Details are given in Ref. [18].

We plan to study conditional quantum feedback in this system, similar to that first demonstrated in Ref. [86], in which the conditional evolution of the atom-cavity system was frozen by application of a control pulse. Compared to the time scale of coherence in that experiment (set by the atom and cavity lifetimes), we have access to ground-state coherences that can last as long as the atom remains in the cavity, which relaxes some of the technical requirements for conditional control. We discuss details of one possible implementation in Ref. [87]. Other possibilities may arise with the additional optical access to the side of the cavity, such as measuring the correlation functions conditioned on a click directly from the (non-collective) atomic emission; this spontaneous emission arises from the same quantum jumps that give the measured light shifts. Another possibility is direct optical manipulation of the atomic states through the side of the cavity, using the output of one of the modes or some auxiliary control field. The flexibility of the system presents many opportunities, some of which are bound to yield even more surprising results.

Bibliography

[1] P. R. Berman, ed., *Cavity Quantum Electrodynamics* (Academic Press, Boston, MA, 1994).

[2] Q. A. Turchette, C. J. Hood, W. Lange, H. Mabuchi, and H. J. Kimble, "Measurement of Conditional Phase Shifts for Quantum Logic," Phys. Rev. Lett. **75**, 4710 (1995).

[3] J. I. Cirac, P. Zoller, H. J. Kimble, and H. Mabuchi, "Quantum State Transfer and Entanglement Distribution among Distant Nodes in a Quantum Network," Phys. Rev. Lett. **78**, 3221 (1997).

[4] K. M. Gheri, C. Saavedra, P. Törmä, J. I. Cirac, and P. Zoller, "Entanglement Engineering of One-Photon Wave Packets Using a Single-Atom Source," Phys. Rev. A **58**, R2627 (1998).

[5] C. Schön, E. Solano, F. Verstraete, J. I. Cirac, and M. M. Wolf, "Sequential Generation of Entangled Multiqubit States," Phys. Rev. Lett. **95**, 110503 (2005).

[6] A. Wallraff, D. I. Schuster, A. Blais, L. Frunzio, R.-S. Huang, J. Majer, S. Kumar, S. M. Girvin, and R. J. Schoelkopf, "Strong Coupling of a Single Photon to a Superconducting Qubit Using Circuit Quantum Electrodynamics," Nature **431**, 162 (2004).

[7] T. Aoki, B. Dayan, E. Wilcut, W. P. Bowen, A. S. Parkins, T. J. Kippenberg, K. J. Vahala, and H. J. Kimble, "Observation of Strong Coupling between One Atom and a Monolithic Microresonator," Nature **443**, 671 (2006).

[8] S. Gleyzes, S. Kuhr, C. Guerlin, J. Bernu, S. Deléglise, U. B. Hoff, M. Brune, J.-M. Raimond and S. Haroche, "Quantum Jumps of Light Recording the Birth and Death of a Photon in a Cavity," Nature **446**, 297 (2007).

[9] M. L. Terraciano, "Cross-Correlations and Entanglement in Cavity QED," Ph. D. Thesis, U of Maryland, College Park, 2006. http://hdl.handle.net/1903/3767

[10] M. L. Terraciano, R. Olson Knell, D. L. Freimund, L. A. Orozco, J. P. Clemens, and P. R. Rice, "Enhanced Spontaneous Emission into the Mode of a Cavity QED System," Opt. Lett. **32**, 982 (2007).

[11] E. T. Jaynes and F. W. Cummings, "Comparison of Quantum and Semiclassical Radiation Theories with Application to the Beam Maser," Proc. IEEE **51**, 89 (1963).

[12] H. J. Carmichael, *An Open Systems Approach to Quantum Optics, Lecture Notes in Physics* **18** (Springer-Verlag, Berlin, 1993).

[13] L. A. Lugiato, "Theory of Optical Bistability," in *Progress in Optics*, **XXI**, 69 (North-Holland, Amsterdam, 1984).

[14] A. T. Rosenberger, L. A. Orozco, H. J. Kimble, and P. D. Drummond, "Absorptive Optical Bistability in Two-State Atoms," Phys. Rev. A **43**, 6284 (1991).

[15] C. J. Hood, M. S. Chapman, T. W. Lynn, and H. J. Kimble, "Real-Time Cavity QED with Single Atoms," Phys. Rev. Lett. **80**, 4157 (1998).

[16] P. Münstermann, T. Fischer, P. Maunz, P. W. H. Pinkse, and G. Rempe, "Dynamics of Single-Atom Motion Observed in a High-Finesse Cavity," Phys. Rev. Lett **82**, 3791 (1999).

[17] G. R. Guthöhrlein, M. Keller, K. Hayasaka, W. Lange, and H. Walther, "A Single Ion as a Nanoscopic Probe of an Optical Field," Nature **414**, 49 (2001).

[18] A. D. Cimmarusti , J. A. Crawford , D. G. Norris, and L. A. Orozco, "Enhancements to Cavity Quantum Electrodynamics System," Rev. Mex. Fis., **TBD** (2011).

[19] Z. T. Lu, K. L. Corwin, M. J. Renn, M. H. Anderson, E. A. Cornell, and C. E. Wieman, "Low-Velocity Intense Source of Atoms from a Magneto-Optical Trap," Phys. Rev. Lett. **77**, 3331 (1996).

[20] R. W. P. Drever, J. L. Hall, F. V. Kowalski, J. Hough, G. M. Ford, A. J. Munley, and H. Ward, "Laser Phase and Frequency Stabilization Using an Optical Resonator," Appl. Phys. B **31**, 97 (1983).

[21] K. L. Corwin, Z. T. Lu, C. F. Hand, R. J. Epstein, and C. E. Wieman, "Frequency-Stabilized Diode Laser with the Zeeman Shift in an Atomic Vapor," Appl. Opt. **37**, 3295 (1998).

[22] L. Isenhower, E. Urban, X. L. Zhang, A. T. Gill, T. Henage, T. A. Johnson, T. G. Walker, and M. Saffman, "Demonstration of a Neutral Atom Controlled-NOT Quantum Gate," Phys. Rev. Lett. **104**, 010503 (2010).

[23] T. Wilk, A. Gatan, C. Evellin, J. Wolters, Y. Miroshnychenko, P. Grangier, and A. Browaeys, "Entanglement of Two Individual Neutral Atoms Using Rydberg Blockade," Phys. Rev. Lett. **104**, 010502 (2010).

[24] N. Schlosser, G. Reymond, I. Protsenko, and P. Grangier, "Sub-Poissonian Loading of Single Atoms in a Microscopic Dipole Trap, Nature **411**, 1024 (2001).

[25] S. Kuhr, W. Alt, D. Schrader, M. Mueller, V. Gomer, and D. Meschede, "Deterministic Delivery of a Single Atom," Science **293**, 278 (2001).

[26] M. P. A. Jones, J. Beugnon, A. Gaëtan, J. Zhang, G. Messin, A. Browaeys, and P. Grangier, "Fast Quantum State Control of a Single Trapped Neutral Atom," Phys. Rev. A **75**, 040301 (R) (2007).

[27] D. A. Lewis, J. F. Tonn, S. L. Kaufman, and G. W. Greenlees, "Photon-Burst Method in High-Resolution Laser Spectroscopy," Phys. Rev. A **19**, 1580 (1979).

[28] K. Peck, L. Stryer, A. N. Glazer, and R. A. Mathies, "Single Molecule Fluorescence Detection: Autocorrelation Criterion and Experimental Realization with Phycoerythrin," Proc. Natl. Acad. Sci. USA **86**, 4087 (1989).

[29] Y.-H. Lee, R. G. Maus, B. W. Smith, and D. Winefordner, "Laser-Induced Fluorescence Detection of a Single Molecule in a Capillary," Anal. Chem. **66**, 4142 (1994).

[30] T. Bondo, M. Hennrich, T. Legero, G. Rempe, and A. Kuhn, "Time-Resolved and State-Selective Detection of Single Freely Falling Atoms, Opt. Comm. **264**, 271 (2006).

[31] E. M. Purcell, Phys. Rev. **69**, 681 (1946).

[32] I. Teper, Y.-J. Lin, and V. Vuleticć, "Resonator-Aided Single-Atom Detection on a Microfabricated Chip," Phys. Rev. Lett. **97**, 023002 (2006).

[33] S. Nussmann, K. Murr, M. Hijlkema, B. Weber, A. Kuhn, and G. Rempe, "Vacuum-Stimulated Cooling of Single Atoms in Three Dimensions," Nature Phys. **1**, 122 (2005).

[34] K. M. Fortier, S. Y. Kim, M. J. Gibbons, P. Ahmadi, and M. S. Chapman, "Deterministic Loading of Individual Atoms to a High-Finesse Optical Cavity," Phys. Rev. Lett. **98**, 233601 (2007).

[35] H. Mabuchi, Q. A. Turchette, M. S. Chapman, and H. J. Kimble, "Real-Time Detection of Individual Atoms Falling through a High-Finesse Optical Cavity," Opt. Lett. **21**, 1393 (1996).

[36] A. Öttl, S. Ritter, M. Köhl, and T. Esslinger, "Correlations and Counting Statistics of an Atom Laser," Phys. Rev. Lett. **95**, 090404 (2005).

[37] M. Trupke, J. Goldwin, B. Darquié, G. Dutier, S. Eriksson, J. Ashmore, and E. A. Hinds, "Atom Detection and Photon Production in a Scalable, Open, Optical Microcavity," Phys. Rev. Lett. **99**, 063601 (2007).

[38] A. D. Boozer, A. Boca, R. Miller, T. E. Northup, and H. J. Kimble, "Cooling to the Ground State of Axial Motion for One Atom Strongly Coupled to an Optical Cavity," Phys. Rev. Lett. **97**, 083602 (2006).

[39] T. Puppe, I. Schuster, A. Grothe, A. Kubanek, K. Murr, P. W. H. Pinkse, and G. Rempe, "Trapping and Observing Single Atoms in a Blue-Detuned Intracavity Dipole Trap," Phys. Rev. Lett. **99**, 013002 (2007).

[40] M. L. Terraciano, R. Olson Knell, D. G. Norris, J. Jing, A. Fernández, and L. A. Orozco, "Photon Burst Detection of Single Atoms in an Optical Cavity," Nat. Phys. **5**, 480 (2009).

[41] K. M. Birnbaum, A. Boca, R. Miller, A. D. Boozer, T. E. Northup, and H. J. Kimble, "Photon Blockade in an Optical Cavity with One Trapped Atom," Nature **436**, 87 (2005).

[42] D. Budker, W. Gawlik, D. F. Kimball, S. M. Rochester, V. V. Yashchuk, and A. Weis, "Resonant Nonlinear Magneto-Optical Effects in Atoms," Rev. Mod. Phys. **74**, 1153 (2002).

[43] L. Mandel and E. Wolf, *Optical Coherence and Quantum Optics* (Cambridge University Press, New York, 1995).

[44] H. J. Kimble, M. Dagenais, and L. Mandel, "Multiatom and Transit-Time Effects on Photon-Correlation Measurements in Resonance Fluorescence," Phys. Rev. A **18**, 201 (1978).

[45] R. Hanbury Brown and R. Twiss, "A Test of a New Type of Stellar Interferometer on Sirius," Nature **178**, 1046 (1956).

[46] H. J. Carmichael, P. Drummond, P. Meystre, and D. F. Walls, "Intensity Correlations in Resonance Fluorescence with Atomic Number Fluctuations," J. Phys. A: Math. Gen. **11** L121 (1978).

[47] H. J. Carmichael, P. D. Drummond, D. F. Walls, and P. Meystre, "Photon Antibunching in Resonance Fluorescence in the Presence of Atomic Number Fluctuations," Optica Acta **27**, 581 (1980).

[48] G. T. Foster, S. L. Mielke, and L. A. Orozco, "Intensity Correlations of a Noise-Driven Diode Laser," J. Opt. Soc. Am. B **15**, 2646 (1998).

[49] M. Hennrich, A. Kuhn, and G. Rempe, "Transition from Antibunching to Bunching in Cavity QED," Phys. Rev. Lett. **94**, 053604 (2005).

[50] G. Labeyrie, C. Miniatura, and R. Kaiser, "Large Faraday Rotation of Resonant Light in a Cold Atomic Cloud," Phys. Rev. A **64**, 033402 (2001).

[51] M. Wilzbach, D. Heine, S. Groth, X. Liu, T. Raub, B. Hessmo, and J. Schmiedmayer, "Simple Integrated Single-Atom Detector," Opt. Lett. **34**, 259 (2009).

[52] P. D. Drummond, "Optical Bistability in a Radially Varying Mode," IEEE J. Quant. Electron. **17**, 301 (1981).

[53] H. J. Carmichael and B. C. Sanders, "Multiatom Effects in Cavity QED with Atomic Beams," Phys. Rev. A **60**, 2497 (1999).

[54] G. Breit, "Quantum Theory of Dispersion (Continued). Parts VI and VII," Rev. Mod. Phys. **5**, 91 (1933).

[55] E. B. Aleksandrov, "Luminescence Beats Induced by Pulsed Excitation of Coherent States," Opt. Spectrosc. **17**, 522 (1964).

[56] J. N. Dodd, W. J. Sandle, and D. Zissermann, "Study of Resonance Fluorescence in Cadmium: Modulation Effects and Lifetime Measurements," Proc. Phys. Soc. **92**, 497 (1967).

[57] A. Aspect, J. Dalibard, P. Grangier, and G. Roger, "Quantum Beats in Continually Excited Atomic Cascades," Opt. Commun. **49**, 429 (1984).

[58] D. G. Norris, L. A. Orozco, P. Barberis-Blostein, and H. J. Carmichael, "Observation of Ground-State Quantum Beats in Atomic Spontaneous Emission," Phys. Rev. Lett. **105**, 123602 (2010).

[59] W. W. Chow, M. O. Scully, and J. O. Stoner Jr, "Quantum-Beat Phenomena Described by Quantum Electrodynamics and Neoclassical Theory," Phys. Rev. A **11**, 1380 (1975).

[60] R. M. Herman, H. Grotch, R. Kornblith, and J. H. Eberly, "Quantum Electrodynamic and Semiclassical Interference Effects in Spontaneous Radiation," Phys. Rev. A **11**, 1389 (1975).

[61] A. T. Forrester, R. A. Gudmundsen, and P. O. Johnson, "Photoelectric Mixing of Incoherent Light," Phys. Rev. **99**, 1691 (1955).

[62] T. Wilk, S. C. Webster, A. Kuhn, and G. Rempe, "Single-Atom Single-Photon Quantum Interface," Science **317**, 488 (2007).

[63] B. Weber, H. P. Specht, T. Müller, J. Bochmann, M. Mücke, D. L. Moehring, and G. Rempe, "Photon-Photon Entanglement with a Single Trapped Atom," Phys. Rev. Lett. **102**, 030501 (2009).

[64] M. Schubert, I. Siemers, R. Blatt, W. Neuhauser, and P. E. Toschek, "Transient Internal Dynamics of a Multilevel Ion," Phys. Rev. A **52**, 2994 (1995).

[65] J. Javanainen, "Effect of State Superpositions Created by Spontaneous Emission on Laser-Driven Transitions," Europhys. Lett. **17**, 407 (1992).

[66] A. K. Patnaik and G. S. Agarwal, "Cavity-Induced Coherence Effects in Spontaneous Emissions from Preselection of Polarization," Phys. Rev. A **59**, 3015 (1999).

[67] S. E. Economou, R.-B. Liu, L. J. Sham, and D. G. Steel, "Unified Theory of Consequences of Spontaneous Emission in a Λ System," Phys. Rev. B **71**, 195327 (2005).

[68] M. Gurudev Dutt, J. Cheng, B. Li, X. Xu, X. Li, P. R. Berman, D. G. Steel, A. S. Bracker, D. Gammon, S. E. Economou, R.-B. Liu, and L. J. Sham, "Stimulated and Spontaneous Optical Generation of Electron Spin Coherence in Charged GaAs Quantum Dots," Phys. Rev. Lett. **94**, 227403 (2005).

[69] A. G. Zajonc, "Proposed Quantum-Beats, Quantum-Eraser Experiment," Phys. Lett. A **96**, 61 (1983).

[70] M. O. Scully and K. Drühl, "Quantum Eraser: A Proposed Photon Correlation Experiment Concerning Observation and "Delayed Choice" in Quantum Mechanics," Phys. Rev. A **25**, 2208 (1982).

[71] L. Horvath and H. J. Carmichael, "Effect of Atomic Beam Alignment on Photon Correlation Measurements in Cavity QED," Phys. Rev. A **76**, 043821 (2007).

[72] L. Allen and J. H. Eberly, *Optical Resonance and Two-Level Atoms* (John Wiley and Sons, Inc., New York, 1975).

[73] H. Dehmelt, Bull. Am. Phys. Soc. **20**, 60 (1975).

[74] R. J. Cook, and H. J. Kimble, "Possibility of Direct Observation of Quantum Jumps," Phys. Rev. Lett. **54**, 1023 (1984).

[75] W. Nagourney, J. Sandberg, and H. Dehmelt, "Shelved Optical Electron Amplifier: Observation of Quantum Jumps," Phys. Rev. Lett. **56**, 2797 (1986).

[76] J. C. Bergquist, R. G. Hulet, W. M. Itano, and D. J. Wineland, "Observation of Quantum Jumps in a Single Atom," Phys. Rev. Lett. **57**, 1699 (1986).

[77] T. Sauter, W. Neuhauser, R. Blatt, and P. E. Toschek, "Observation of Quantum Jumps," Phys. Rev. Lett. **57**, 1696 (1986).

[78] W. Happer, "Light Propagation and Light Shifts in Optical Pumping Experiments," Prog. Quant. Electron. **1**, 51 (1970).

[79] R. A. Cline, J. D. Miller, M. R. Matthews, and D. J. Heinzen, "Spin Relaxation of Optically Trapped Atoms by Light Scattering," Opt. Lett. **19**, 207 (1994).

[80] R. Ozeri, C. Langer, J. D. Jost, B. DeMarco, A. Ben-Kish, B. R. Blakestad, J. Britton, J. Chiaverini, W. M. Itano, D. B. Hume, D. Leibfried, T. Rosenband, P. O. Schmidt, and D. J. Wineland, "Hyperfine Coherence in the Presence of Spontaneous Photon Scattering," Phys. Rev. Lett. **95**, 030403 (2005).

[81] H. Uys, M. J. Biercuk, A. P. VanDevender, C. Ospelkaus, D. Meiser, R. Ozeri, and J. J. Bollinger, "Decoherence Due to Elastic Rayleigh Scattering, Phys. Rev. Lett. **105**, 200401 (2010).

[82] C. Cohen-Tannoudji, *Ann. Phys. (Paris), 13e série* **7**, 423 (1962).

[83] A. Kastler, "Displacement of Energy Levels of Atoms by Light," J. Opt. Soc. Am. **53**, 902 (1963).

[84] B. R. Bulos, A. Marshall, and W. Happer, "Light Shifts Due to Real Transitions in Optically Pumped Alkali Atoms," Phys. Rev. A **4**, 51 (1971).

[85] J. C. Lehmann, "Nuclear Orientation of Cadmium^{111} by Optical Pumping with the Resonance Line 5^1S_0-5^1P_1," Phys. Rev. **178**, 153 (1969).

[86] W. P. Smith, J. E. Reiner, L. A. Orozco, S. Kuhr, and H. M. Wiseman, "Capture and Release of a Conditional state of a Cavity QED System by Quantum Feedback," Phys. Rev. Lett. **89**, 133601 (2002).

[87] P. Barberis-Blostein, D. G. Norris, L. A. Orozco, and H. J. Carmichael, "From Quantum Feedback to Probabilistic Error Correction: Manipulation of Quantum Beats in Cavity QED," New J. of Phys. **12**, 023002 (2010).